Weak-coupling continuous-time quantum Monte Carlo study of the single impurity and periodic Anderson models with *s*-wave superconducting baths

David J. Luitz[*] and Fakher F. Assaad

Institut für Theoretische Physik und Astrophysik, Universität Würzburg, 97074 Würzburg, Germany
(Received 22 September 2009; revised manuscript received 30 November 2009; published 12 January 2010)

We apply the unbiased weak-coupling continuous time quantum Monte Carlo method to review the physics of a single magnetic impurity coupled to *s*-wave superconducting leads described by the BCS reduced Hamiltonian. As a function of the superconducting gap Δ, we study the signature of the first-order transition between the singlet and doublet (local-moment) states on various quantities. In particular, we concentrate on the Josephson current with 0 to π phase shift, the crossing of the Andreev bound states in the single-particle spectral function, as well as the local dynamical spin structure factor. Within dynamical mean-field theory, this impurity problem provides a link to the periodic Anderson model (PAM) with superconducting conduction electrons (BCS-PAM). The first-order transition observed in the impurity model is reproduced in the BCS-PAM and is signalized by the crossing of the low-energy excitations in the local density of states. The momentum resolved single-particle spectral function in the singlet state reveals the coherent, Bloch-type, superposition of Andreev bound states. In the doublet or local-moment phase the single-particle spectral function is characterized by incoherent quasiparticle excitations.

I. INTRODUCTION

Magnetic degrees of freedom in superconducting environments have attracted considerable interest due to the underlying competing effects. Already a classical spin oriented along the *z* axis[1,2] embedded in a superconducting host generates a localized state within the superconducting gap. As a function of the interaction strength this excitation crosses the Fermi energy thereby triggering a first-order transition between a ground state with vanishing total electronic spin and a ground state with nonzero total electronic spin.

For a quantum spin, the Kondo effect sets in. Being a Fermi-surface instability, the opening of the superconducting gap competes with Kondo screening and ultimately leads to a local-moment regime. This transition is accompanied by a 0 to π phase shift in the Josephson current. In the local-moment regime the π shift occurs since a Cooper pair tunneling through the junction necessarily accumulates a phase π.[3–6]

The interest in the problem has been renewed in the last decade by the rapid progress in nanotechnology which made a direct experimental realization of quantum dots coupled to superconducting leads feasible so that many experiments have been designed to directly measure the 0 to π transition of the Josephson current. Experiments using a carbon nanotube[7–9] but also InAs nanowires[10] as a quantum dot coupled to superconducting leads were able to observe the sign change in the Josephson current by increasing the gate voltage and thus manipulating the number of electrons on the quantum dot. The effect of the changing electron number on the behavior of such systems has been extensively studied[11–14] and the theoretical expectation of the collapse of the Kondo effect if the superconducting gap Δ exceeds the Kondo temperature T_K has been confirmed by experiments of Buitelaar *et al.*[15]

From the numerical point of view, a combination of algorithmic development and computational power has allowed for a more detailed study of the problem using the numerical renormalization group (NRG),[16–19] quantum Monte Carlo simulations[20–22] as well as functional renormalization group (fRG) calculations.[23] Most numerical works present in the literature only present either the study of the Josephson current[16,20,21,23] or the study of the spectral properties of the Quantum dot.[18] One of the goals of this paper is to use the weak-coupling continuous time quantum Monte Carlo (CTQMC) method[24] to compute the Josephson current as well as the spectral functions for the same parameter set in order to present a comprehensive study of the 0 to π transition of a Josephson quantum dot. Our numerically exact data clearly confirms the picture of a first-order phase transition from a singlet phase linked to the 0-junction regime of the Josephson current to a doublet phase corresponding to the π-junction regime.

In addition to numerical efforts, many analytical approximations have been introduced to tackle different aspects of the physics of the problem. The noncrossing approximation has been used to show that Andreev bound states crossing the Fermi energy are connected to the 0 to π transition of the Josephson current.[25] Perturbative methods as well as mean-field theory have brought a quite complete understanding of the phase diagram featuring the 0 and π phases as well as the intermediate phases $0'$ and π'.[26–28] Another method employed by several authors is the introduction of different analytically solvable effective models, which are valid in different limits.[18,27,28] These models are very useful to acquire an intuitive understanding of the physics. We will present the study of an effective Hamiltonian for the limit of a superconducting gap Δ much larger than the bandwidth to support the interpretation of the CTQMC data.

Another motivation of this paper is to study within dynamical mean-field theory (DMFT) (Ref. 29) the periodic Anderson model with an *s*-wave BCS-conduction band (BCS-PAM). Within this approximation, the BCS-PAM maps onto the single impurity Anderson model with superconduct-

ing baths supplemented with a self-consistency condition. We will show that the physics of the impurity model can be taken over to the lattice case. In particular, the first-order transition observed in the impurity model is reproduced in the BCS-PAM and is signalized by the crossing of the low-energy excitations in the local density of states. The momentum resolved single-particle spectral function in the singlet phase reveals the coherent, Bloch-type, superposition of Andreev bound states. In the doublet or local-moment phase the single-particle spectral function is characterized by incoherent quasiparticle excitations. We provide an understanding of this in terms of models of disorder.

The paper is organized as follows. After introducing the model in Sec. II, we discuss in Sec. III an effective toy model valid in the limit of a superconducting gap, Δ, much larger than the bandwidth W. This simple toy model goes a good way at understanding certain aspects of the underlying physics. A brief outline of the employed CTQMC result including the proof of Wick's theorem for each configuration in the Monte Carlo simulation will be presented in Sec. IV. The results of the toy model are then compared to the results of the CTQMC simulation, which are discussed in detail in Sec. V. Section VI is dedicated to the study of the BCS-PAM within DMFT. We include the Appendix featuring the proof of a general determinant identity needed for the proof of Wick's theorem for every configuration in the CTQMC.

II. MODEL

The physics of a quantum dot coupled to two superconducting leads with N lattice sites (L=left,R=right) via a hybridization term is captured by the single impurity Anderson model with the leads described by the BCS mean-field Hamiltonian,

$$\widetilde{H} = \sum_{\alpha=L}^{R} \widetilde{H}_{0,\alpha} + \widetilde{H}_d + \widetilde{H}_V \tag{1}$$

with

$$\widetilde{H}_{0,\alpha} = \sum_{k,\sigma} \xi_k \widetilde{c}_{k,\sigma,\alpha}^\dagger \widetilde{c}_{k,\sigma,\alpha} - \sum_k (\Delta e^{i\phi_\alpha} \widetilde{c}_{k,\uparrow,\alpha}^\dagger \widetilde{c}_{-k,\downarrow,\alpha}^\dagger + \text{H.c.}),$$

$$\widetilde{H}_d = \sum_\sigma \xi_d \widetilde{d}_\sigma^\dagger \widetilde{d}_\sigma + U \left(\widetilde{d}_\uparrow^\dagger \widetilde{d}_\uparrow - \frac{1}{2} \right) \left(\widetilde{d}_\downarrow^\dagger \widetilde{d}_\downarrow - \frac{1}{2} \right),$$

$$\widetilde{H}_V = -\frac{V}{\sqrt{N}} \sum_{\alpha=L}^{R} \sum_{\sigma,k} (\widetilde{c}_{k,\sigma,\alpha}^\dagger \widetilde{d}_\sigma + \widetilde{d}_\sigma^\dagger \widetilde{c}_{k,\sigma,\alpha}). \tag{2}$$

The operators $\widetilde{c}_{k,\sigma,\alpha}^\dagger$ are creation operators for electrons with a z component of the spin σ and momentum k in lead α, $\widetilde{d}_\sigma^\dagger$ is a creation operator of an electron with a z component of the spin σ on the quantum dot. $\xi_k = \epsilon(k) - \mu = -2t \cos(k) - \mu$ is the dispersion relation for the electrons in the leads, where we assume that the dispersion is independent of the lead index α and $\xi_d = \epsilon_d - \mu$ is the position of the dot level. Throughout this paper, we will express all quantities in units of t=1. The superconducting order parameter has a modulus

Δ and a phase ϕ_α. The parameter V characterizes the strength of the hybridization and U corresponds to the Coulomb blockade.

Since the Hamiltonian does not conserve the electron number as a consequence of the BCS term, we use the standard trick of rewriting the Hamiltonian in terms of creation and annihilation operators of quasiparticles, which for spin up are identical to the electrons but correspond to holes in the spin-down sector. This can also be expressed as a canonical transformation,

$$\widetilde{d}_\uparrow^\dagger \to d_\uparrow^\dagger, \ \ \widetilde{d}_\downarrow^\dagger \to d_\downarrow, \ \ \widetilde{c}_{k,\uparrow,\alpha}^\dagger \to c_{k,\uparrow,\alpha}^\dagger, \ \ \widetilde{c}_{-k,\downarrow,\alpha}^\dagger \to c_{k,\downarrow,\alpha}. \tag{3}$$

Using the new operators, the Hamiltonian can be written in a Nambu notation,

$$H = H_0 + H_U = \sum_{k,\alpha} \mathbf{c}_{k,\alpha}^\dagger \mathbf{E}_\alpha(k) \mathbf{c}_{k,\alpha} + \mathbf{d}^\dagger \epsilon_d \mathbf{d}$$

$$-\frac{V}{\sqrt{N}} \sum_{k,\alpha} (\mathbf{c}_{k,\alpha}^\dagger \sigma_z \mathbf{d} + \mathbf{d}^\dagger \sigma_z \mathbf{c}_{k,\alpha}) + H_U \tag{4}$$

with $H_U = -U(d_\uparrow^\dagger d_\uparrow - \frac{1}{2})(d_\downarrow^\dagger d_\downarrow - \frac{1}{2})$, the Nambu spinors

$$\mathbf{d} = \begin{pmatrix} d_\uparrow \\ d_\downarrow \end{pmatrix}, \ \ \mathbf{c}_{k,\alpha} = \begin{pmatrix} c_{k,\uparrow,\alpha} \\ c_{k,\downarrow,\alpha} \end{pmatrix}, \tag{5}$$

the matrices

$$\mathbf{E}_\alpha(k) = \begin{pmatrix} \xi_k & -\Delta e^{i\phi_\alpha} \\ -\Delta e^{-i\phi_\alpha} & -\xi_k \end{pmatrix}, \ \ \epsilon_d = \begin{pmatrix} \xi_d & 0 \\ 0 & -\xi_d \end{pmatrix}, \tag{6}$$

and the Pauli matrix

$$\sigma_z = \begin{pmatrix} 1 & 0 \\ 0 & -1 \end{pmatrix}. \tag{7}$$

For practical reasons, we use the following definition for the single-particle Green's function throughout Secs. II–V:

$$G_{dd}^{\sigma\sigma'}(i\omega_m) = \int_0^\beta d\tau \exp(i\omega_m \tau) \langle T d_\sigma^\dagger(\tau) d_{\sigma'} \rangle. \tag{8}$$

With this definition, the resolvent operator $\mathbf{G}^0(i\omega_m) = (-i\omega_m \mathbf{1} - \mathbf{H}_0^T)^{-1}$ can be used to obtain the Green's function of the noninteracting system,

$$\mathbf{G}_{dd}^0(i\omega_n)^{-1} = (-i\omega_n \mathbf{1} - \epsilon_d) + \frac{V^2}{N} \sum_{\alpha,k} \sigma_z [i\omega_n \mathbf{1} + \mathbf{E}_\alpha^T(k)]^{-1} \sigma_z. \tag{9}$$

III. EFFECTIVE HAMILTONIAN IN THE LIMIT $\Delta/W \to \infty$

To gain a deeper understanding of the physics on the quantum dot, it is useful to search for analytically solvable toy models. We will study an effective model, which reproduces the physics of Hamiltonian (1) in the limit $\Delta/W \to \infty$, where W is the bandwidth. To derive the effective model, we look at the limit $\Delta \to \infty$ of the Green's function in Eq. (9). The superconducting order parameter Δ appears only in the

matrix $\mathbf{E}_\alpha(k)$, thus we examine the behavior of this matrix for large values of Δ. This can easily be done by diagonalizing $\mathbf{E}_\alpha(k)$ for $\phi_\alpha = 0$,

$$\mathbf{E}_\alpha(k) = \mathbf{U}_\Delta^{-1}\begin{pmatrix} -\sqrt{\Delta^2 + \xi_k^2} & 0 \\ 0 & \sqrt{\Delta^2 + \xi_k^2} \end{pmatrix}\mathbf{U}_\Delta. \quad (10)$$

Let us first look at the limit $\Delta \to \infty$ of the transformation matrix U_Δ, which for brevity is not a unitary matrix,

$$\mathbf{U}_\Delta = \begin{pmatrix} -\dfrac{\xi_k - \sqrt{\Delta^2 + \xi_k^2}}{\Delta} & 1 \\ -\dfrac{\xi_k + \sqrt{\Delta^2 + \xi_k^2}}{\Delta} & 1 \end{pmatrix} \Rightarrow \mathbf{U}_\infty = \begin{pmatrix} 1 & 1 \\ -1 & 1 \end{pmatrix}. \quad (11)$$

The diagonal matrix in Eq. (10) can be considered in a similar manner and we obtain for $\lim\limits_{\Delta \to \infty} \mathbf{E}_\alpha(k) = \mathbf{E}_\infty$,

$$\mathbf{E}_\infty = \mathbf{U}_\infty^{-1}\begin{pmatrix} -\Delta & 0 \\ 0 & \Delta \end{pmatrix}\mathbf{U}_\infty = \begin{pmatrix} 0 & -\Delta \\ -\Delta & 0 \end{pmatrix}. \quad (12)$$

Using this result, for large values of Δ the sum over k and α in Eq. (9) can be carried out yielding

$$\mathbf{G}_{dd}^{0,\infty}(i\omega_n)^{-1} = (-i\omega_n\mathbf{1} - \epsilon_d) + 2V^2\sigma_z(i\omega_n\mathbf{1} + \mathbf{E}_\infty)^{-1}\sigma_z. \quad (13)$$

This is exactly the free Green's function obtained from a Hamiltonian of the form

$$H_{\text{eff}} = -\sqrt{2}V(\mathbf{c}^\dagger\sigma_z\mathbf{d} + \mathbf{d}^\dagger\sigma_z\mathbf{c}) + \mathbf{c}^\dagger\mathbf{E}_\infty\mathbf{c} + \mathbf{d}^\dagger\epsilon_d\mathbf{d} + H_U, \quad (14)$$

where H_{eff} describes a system consisting of one bath site c connected by a hybridization term to the correlated quantum dot d. The dispersion of the bath has completely vanished, as the superconducting band gap becomes much larger than the bandwidth.

We chose a basis of the 16 dimensional Hilbert space and write the Hamiltonian as a matrix, which subsequently can be diagonalized. As we have restricted the parameter space for the Monte Carlo simulations to $\epsilon_d = 0$ and $\mu = 0$ in the original Hamiltonian of Eq. (1), we will use the same parameters for the exact diagonalization results.

Note that the effective Hamiltonian in the limit Δ/W is not unique. In the case of real Δ, the Green's function in Eq. (9) for $N = 1$, $\mu = -2t$, and $\epsilon_d = \mu$ reduces exactly to Eq. (13), as $\mathbf{E}_L = \mathbf{E}_R = \mathbf{E}_\infty$. This case corresponds to the effective Hamiltonian in the zero bandwidth limit studied by Vecino et al.[27]

A. Ground state of the effective model

The ground state of the system [Eq. (14)] can be determined by diagonalizing the Hamiltonian H_{eff}. As depicted in Fig. 1, the energy levels cross at a critical value of $U = U_c$ and a similar behavior can be observed by varying Δ with a corresponding critical value Δ_c. For $U < U_c$ and $\Delta < \Delta_c$, the ground state is given by $|\psi_s\rangle = -\alpha(|\uparrow\downarrow,0\rangle - |0,\uparrow\downarrow\rangle) - \beta(|\uparrow,\downarrow\rangle + |\downarrow,\uparrow\rangle) - \gamma(|\downarrow,\downarrow\rangle + |\uparrow,\uparrow\rangle)$, with the notation
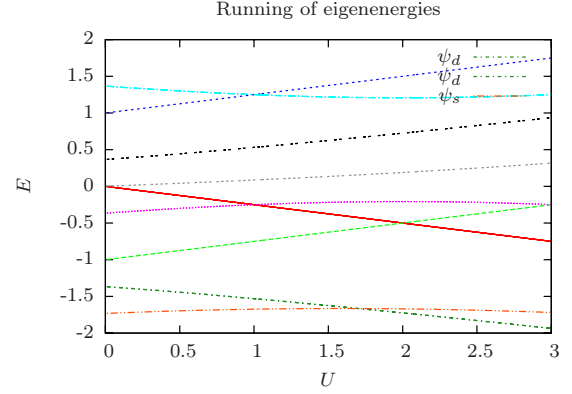

FIG. 1. (Color online) Eigenenergies of the effective Hamiltonian (14) for varying U. The fixed parameters are given by $V = 0.5$ and $\Delta = 1$. The crossing of the two lowest levels is clearly seen at $U \approx 1.7$. The ground state for $U < 1.7$ is a singlet state. For larger values of U, the twofold-degenerate doublet state becomes energetically more favorable.

$c_\sigma^\dagger|0,0\rangle = |\sigma,0\rangle$ and $d_\sigma^\dagger|0,0\rangle = |0,\sigma\rangle$. Note that we are using the unphysical basis introduced in Eq. (3). To interpret this ground state it is better to return to the physical basis by inverting the canonical transformation in Eq. (3) and transforming the vacuum state $|0,0\rangle \to |\widetilde{\downarrow},\widetilde{\downarrow}\rangle$. The ground state can then be rewritten in the physical basis as

$$|\psi_s\rangle = \alpha(|\widetilde{\downarrow},\widetilde{\uparrow}\rangle - |\widetilde{\uparrow},\widetilde{\downarrow}\rangle) + \beta(|\widetilde{0},\widetilde{\uparrow\downarrow}\rangle + |\widetilde{\uparrow\downarrow},\widetilde{0}\rangle)$$
$$+ \gamma(|\widetilde{0},\widetilde{0}\rangle + |\widetilde{\uparrow\downarrow},\widetilde{\uparrow\downarrow}\rangle). \quad (15)$$

This state is clearly a singlet state, corresponding to a Kondo singlet between the quantum dot and the bath with the dominant weight α. The states representing a pairing on the quantum dot or in the bath have the suppressed weights β and γ for small values of Δ but grow more important if Δ is increased as is shown in Fig. 2.

At $U > U_c$, the ground state changes and we get the twofold-degenerate ground states $|\psi_{d,\uparrow}\rangle = a(|\uparrow\downarrow,\uparrow\rangle - |\uparrow\downarrow,\downarrow\rangle) + b(|\uparrow,\uparrow\downarrow\rangle + |\downarrow,\uparrow\downarrow\rangle)$ and $|\psi_{d,\downarrow}\rangle = a(|0,\uparrow\rangle - |0,\downarrow\rangle) + b(|\downarrow,0\rangle + |\uparrow,0\rangle)$, rewritten in the physical basis,

$$|\psi_{d,\uparrow}\rangle = a(|\widetilde{\uparrow},\widetilde{0}\rangle - |\widetilde{\uparrow},\widetilde{\uparrow\downarrow}\rangle) + b(|\widetilde{0},\widetilde{\uparrow}\rangle + |\widetilde{\uparrow\downarrow},\widetilde{\uparrow}\rangle),$$

$$|\psi_{d,\downarrow}\rangle = a(|\widetilde{\downarrow},\widetilde{0}\rangle - |\widetilde{\downarrow},\widetilde{\uparrow\downarrow}\rangle) + b(|\widetilde{0},\widetilde{\downarrow}\rangle + |\widetilde{\uparrow\downarrow},\widetilde{\downarrow}\rangle). \quad (16)$$

This twofold-degenerate ground state has a z component of the total spin $\pm 1/2$ and hence corresponds to a local moment.

B. Phase diagram

To further illustrate the phase transition between the singlet state $|\psi_s\rangle$ and the doublet states $|\psi_{d,\uparrow\downarrow}\rangle$, the double occupancy $\langle \widetilde{d}_\uparrow^\dagger \widetilde{d}_\uparrow \widetilde{d}_\downarrow^\dagger \widetilde{d}_\downarrow \rangle$ of the quantum dot in the effective model is shown in Fig. 3. At low temperature a very sharp drop of the double occupancy on the phase boundary can be observed, which evolves to a jump at $T = 0$. Here the larger values of the double occupancy are connected to the singlet
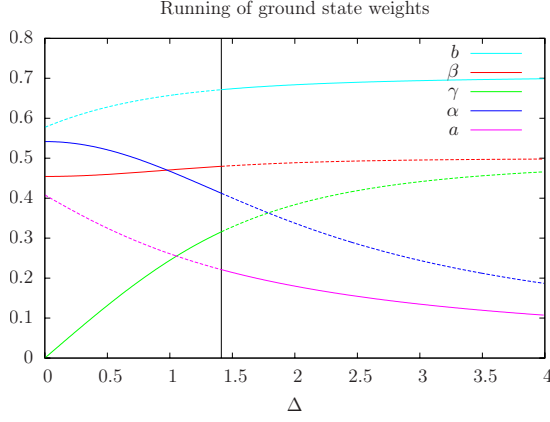
Running of ground state weights

FIG. 2. (Color online) For $\Delta < 1.412$ the ground state is the singlet state from Eq. (15). If Δ is increased, the weight α of the single occupied states $|\tilde{\uparrow}, \tilde{\downarrow}\rangle$ and $|\tilde{\downarrow}, \tilde{\uparrow}\rangle$ decreases in favor of the states with a double occupied quantum dot, corresponding to the weights β and γ. At $\Delta = 1.412$ the ground state changes to the twofold-degenerate doublet state given in Eq. (16) and the weight of the states with a single occupied quantum dot b increases with Δ. The parameters in this plot are $V = 0.5$ and $U = 1.0$.

phase while the lower values belong to the doublet phase, where single occupancy is favored. This can be understood by studying the expectation value of the double occupancy in the ground state. In the singlet phase, we obtain

$$\langle \psi_s | \tilde{d}_\uparrow^\dagger \tilde{d}_\uparrow \tilde{d}_\downarrow^\dagger \tilde{d}_\downarrow | \psi_s \rangle = |\beta|^2 + |\gamma|^2 \quad (17)$$

and for the doublet phase,

$$\langle \psi_{d,\uparrow\downarrow} | \tilde{d}_\uparrow^\dagger \tilde{d}_\uparrow \tilde{d}_\downarrow^\dagger \tilde{d}_\downarrow | \psi_{d,\uparrow\downarrow} \rangle = |a|^2. \quad (18)$$

From the behavior of the weights β, γ, and a shown in Fig. 2 it is clear that the double occupancy increases with Δ in the singlet phase and decreases in the doublet phase. Note that many of the results presented in this paper can be observed either at fixed U or Δ as can be conjectured from Fig. 3.
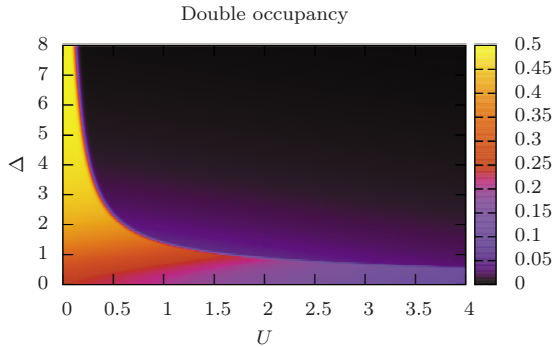
Double occupancy

FIG. 3. (Color online) Double occupancy $\langle \tilde{d}_\uparrow^\dagger \tilde{d}_\uparrow \tilde{d}_\downarrow^\dagger \tilde{d}_\downarrow \rangle$ of the quantum dot in the effective model at $\beta = 200$ and $V = 0.5$. This plot can be understood as a phase diagram of the effective model, as the phase boundary is accompanied by a sharp decay of the double occupancy.

C. Proximity effect

To gain further insight in the sign change in the local pair correlations $\langle \tilde{d}_\uparrow^\dagger \tilde{d}_\downarrow^\dagger \rangle$,[16,30,31] we calculate the ground-state expectation value of the local pair correlations in the effective model (14). For the singlet phase, we obtain

$$\langle \psi_s | \tilde{d}_\uparrow^\dagger \tilde{d}_\downarrow^\dagger | \psi_s \rangle = \langle \psi_s | (\beta | \tilde{\uparrow}\tilde{\downarrow}, \tilde{\uparrow}\tilde{\downarrow} \rangle + \gamma | \tilde{\uparrow}\tilde{\downarrow}, \tilde{0} \rangle) = 2 \, \text{Re}(\beta^* \gamma) \geq 0. \quad (19)$$

Clearly, only terms describing the pairing on the quantum dot contribute to the pair correlations, whereas the Kondo singlet of electrons on the quantum dot and in the bath does not. From Fig. 2, it is obvious that the resulting pairing correlation is positive and increases with Δ. This illustrates the proximity effect, as a pair field in the bath induces a pair field on the quantum dot.

On the other hand, in the doublet phase, we obtain

$$\langle \psi_{d,\downarrow} | \tilde{d}_\uparrow^\dagger \tilde{d}_\downarrow^\dagger | \psi_{d,\downarrow} \rangle = \langle \psi_{d,\downarrow} | a | \tilde{\downarrow}, \tilde{\uparrow}\tilde{\downarrow} \rangle = -|a|^2 < 0. \quad (20)$$

As in the singlet phase, only the states corresponding to a pairing on the quantum dot contribute to the pair correlations. The local-moment part of the ground state does not generate pair correlations. As the weight a in the doublet-phase ground state is positive and decreases with Δ (see Fig. 2), the local pair correlations have a negative sign in contrast to the positive sign in the singlet phase and decrease with Δ.

D. Spectral function

Using the Lehmann representation, the spectral function $A_{\uparrow\uparrow}(\omega)$ of the effective model is easily calculated. It is defined by

$$A_{\uparrow\uparrow}(\omega) = \frac{\pi}{Z} \sum_{n,m} M_{nm} (e^{-\beta E_m} + e^{-\beta E_n}) \delta(\omega + E_n - E_m) \quad (21)$$

with the matrix elements $M_{nm} = |\langle n | \tilde{d}_\uparrow^\dagger | m \rangle|^2$. The spectral function is shown in Fig. 4. Comparing this plot to the numerical solution of the full model as depicted in Fig. 14, we observe that the simple model already shows the important feature of an excitation at the position $\omega = 0$ at the critical value of Δ. Even though for very small values of Δ, the Kondo resonance at $\omega = 0$ cannot be seen in the simple model, we see a precursor of the Kondo resonance as a pole of the Green's function, which develops into a resonance if we increase the number of sites in the bath.[32]

A careful analysis reveals that the low-frequency signature of the spectral function reflects the excitation between the two lowest lying states of the spectrum. These states are the ground states of the singlet and the doublet phases and therefore, the position ω of the excitation marks precisely the energy difference of the two ground states. At the critical value of $\Delta = 1.412$, the level crossing occurs and leads to a vanishing energy difference of the two ground states, meaning that the excitation between the two states lies now precisely at $\omega = 0$.
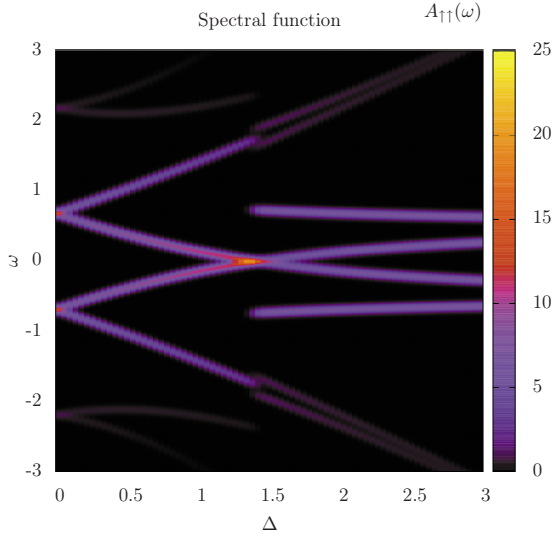
FIG. 4. (Color online) Spectral function $A_{\uparrow\uparrow}(\omega)$ of the effective model for different values of Δ at $\beta=200$, $U=1$, and $V=0.5$. The δ peaks have been broadened by a Gaussian function of width $\sigma=0.04$ for better visibility.

E. Dynamical spin structure

Like the spectral function, the dynamical spin structure factor $S(\omega)$ can be calculated using the Lehmann representation,

$$S(\omega) = \frac{\pi}{Z} \sum_{n,m} e^{-\beta E_n} |\langle n|\widetilde{S}_+|m\rangle|^2 \delta(\omega + E_n - E_m). \quad (22)$$

In the Monte Carlo simulation, a numerically more stable quantity is obtained by replacing S_+ by S_z in the above equation. This quantity is completely equivalent to $S(\omega)$, as we only make use of the SU(2) symmetry of the problem and is therefore used in the following.

In the representation [Eq. (22)] of $S(\omega)$, it is clear that the dynamical spin structure factor will show excitations at frequencies corresponding to the energy needed to flip the spin on the quantum dot. Therefore, the dynamical spin structure factor is very well suited to determine whether the system is in the singlet or in the doublet regime. In Fig. 5 the phase transition from the singlet phase to the doublet phase is reflected by the fact that in the singlet phase, a gapped excitation can be observed, whereas in the doublet phase, a peak at $\omega=0$ emerges, which corresponds to a local magnetic moment.

F. Dynamical charge structure

The dynamical charge structure factor $N(\omega)$ can be defined by the Lehman representation,

$$N(\omega) = -\frac{\pi}{Z} \sum_{n,m} |\langle n|\widetilde{n} - \delta_{n,m}|m\rangle|^2 e^{-\beta E_m} \delta(\omega + E_n - E_m). \quad (23)$$

As for the other spectral functions, the charge structure factor $N(\omega)$ shown in Fig. 6 exhibits a sharp change in its
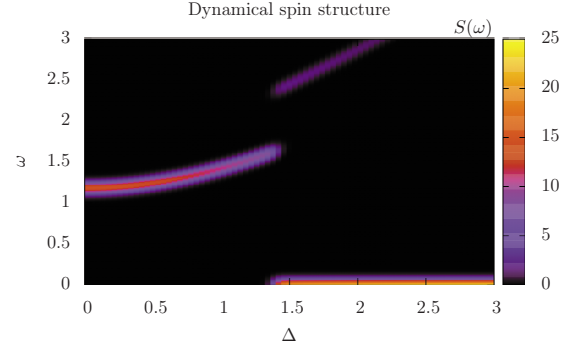

FIG. 5. (Color online) Dynamical spin structure factor $S(\omega)$ of the effective model at $\beta=200$. The phase transition from the singlet phase to the doublet phase for $U=1$ and $V=0.5$ occurs at $\Delta \approx 1.412$. At this point a transition from a gapped excitation to a peak at $\omega=0$ corresponding to a local magnetic moment in the doublet phase is observed. To visualize the δ functions, a Gaussian broadening of width $\sigma=0.05$ has been applied.

behavior at the phase transition for the critical value of the superconducting gap Δ. We observe that the charge structure shows a finite gap for all values of Δ and that for large values of Δ, the gap increases in a slightly nonlinear manner.

A more detailed study of the matrix elements contributing to the charge structure factor reveals that because of correlation we have completely different excitations than for the spectral function. In fact, the most prominent excitations are excitations from the respective ground states in the two different phases to higher energy states with structure similar to that of the ground states.

IV. CTQMC

A. Basic outline of the algorithm

For the numerically exact solution of the BCS-Anderson model, we used the weak-coupling CTQMC method,[24] which is based on a perturbation expansion around the limit of $U=0$. Following the presentation of the CTQMC algorithm in Ref. 33, we will shortly outline the basic principles of the method.

As pointed out in Refs. 24 and 33 the interacting Hamiltonian H_U in Eq. (4) can up to a constant be rewritten as
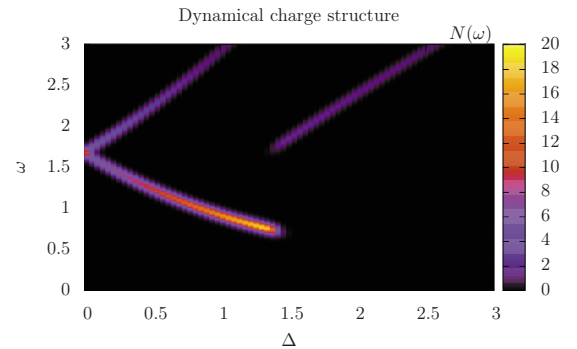

FIG. 6. (Color online) Dynamical charge structure factor $N(\omega)$ of the effective model at $\beta=200$. We have used the same parameters as for Fig. 4.

$$H_U = -\frac{U}{2} \sum_{s=\pm 1} (d_\uparrow^\dagger d_\uparrow - \alpha_\uparrow^s)(d_\downarrow^\dagger d_\downarrow - \alpha_\downarrow^s) \qquad (24)$$

introducing the parameters α_σ^s to minimize the sign problem. For the present case, a choice of $\alpha_\uparrow^s = \alpha_\downarrow^s = \frac{1}{2} + s\delta$ with $\delta = \frac{1}{2} + 0^+$ was found to completely eliminate the sign problem at half filling, even after the complex phase factors $\exp(i\phi_\alpha)$ in the Hamiltonian were introduced.

Using perturbation theory, the partition function Z of the full Hamiltonian (4) can be written as

$$\frac{Z}{Z_0} = \left\langle Te^{-\int_0^\beta d\tau H_U(\tau)} \right\rangle_0 = \sum_{n=0}^\infty \left(\frac{U}{2}\right)^n \int_0^\beta d\tau_1 \cdots \int_0^{\tau_{n-1}} d\tau_n \sum_{s_1,\ldots,s_n}$$
$$\times \langle T[\hat{n}_\uparrow(\tau_1) - \alpha_\uparrow^{s_1}] \cdots [\hat{n}_\downarrow(\tau_n) - \alpha_\downarrow^{s_n}] \rangle_0 \qquad (25)$$

with the number operators $\hat{n}_\sigma = d_\sigma^\dagger d_\sigma$ and the thermal expectation value $\langle \bullet \rangle_0 = \frac{1}{Z_0} \mathrm{Tr}[e^{-\beta H_0} \bullet]$. As H_0 is a noninteracting Hamiltonian, Wick's theorem holds and the expectation value $\langle T[\hat{n}_\uparrow(\tau_1) - \alpha_\uparrow^1] \cdots [\hat{n}_\downarrow(\tau_n) - \alpha_\downarrow^n] \rangle_0$ can be cast in a determinant of a matrix $\mathbf{M}_{C_n}$ of size $2n \times 2n$, where C_n is a configuration of vertices $\{\tau_i, s_i\}$. In contrast to the formulation for the Hubbard model given in Ref. 33, we do not need to include an index for the lattice site as we only have one correlated site, the impurity. The matrix $\mathbf{M}_{C_n}$ is not block diagonal for the two spin sectors in the case $\Delta \neq 0$, so we cannot factor the determinant in two determinants of $n \times n$ matrices. Finally, the partition function of the model is given by

$$\frac{Z}{Z_0} = \sum_{C_n} \left(\frac{U}{2}\right)^n \det \mathbf{M}_{C_n}, \qquad (26)$$

where the sum runs over all possible configurations C_n of vertices as in Ref. 33. The matrix $\mathbf{M}_{C_n}$ is defined by

$$\mathbf{M}_{C_n} = \begin{pmatrix} \mathbf{G}_{dd}^0(\tau_1, \tau_1) - \alpha_1 & \cdots & \mathbf{G}_{dd}^0(\tau_n, \tau_1) \\ \vdots & \ddots & \vdots \\ \mathbf{G}_{dd}^0(\tau_1, \tau_n) & \cdots & \mathbf{G}_{dd}^0(\tau_n, \tau_n) - \alpha_n \end{pmatrix} \qquad (27)$$

using the 2×2 Green's function matrices $\mathbf{G}_{dd}^0(\tau, \tau') = \begin{pmatrix} \langle Td_\uparrow^\dagger(\tau)d_\uparrow(\tau') \rangle_0 & \langle Td_\uparrow^\dagger(\tau)d_\downarrow(\tau') \rangle_0 \\ \langle Td_\downarrow^\dagger(\tau)d_\uparrow(\tau') \rangle_0 & \langle Td_\downarrow^\dagger(\tau)d_\downarrow(\tau') \rangle_0 \end{pmatrix}$ and with $\alpha_i = \begin{pmatrix} \alpha_i^\uparrow & 0 \\ 0 & \alpha_i^\downarrow \end{pmatrix}$.

A similar reasoning yields an expression for the thermal expectation value $\langle O(\tau) \rangle = \frac{1}{Z} \mathrm{Tr}[e^{-\beta H} O(\tau)]$ of the full model,

$$\langle O(\tau) \rangle = \frac{\sum_{C_n} \left(\frac{U}{2}\right)^n \det \mathbf{M}_{C_n} \langle\langle O(\tau) \rangle\rangle_{C_n}}{\sum_{C_n} \left(\frac{U}{2}\right)^n \det \mathbf{M}_{C_n}}. \qquad (28)$$

Here $\langle\langle O(\tau) \rangle\rangle_{C_n}$ is the contribution of the configuration C_n to the observable $O(\tau)$, which is given by

$$\langle\langle O(\tau) \rangle\rangle_{C_n} = \frac{\langle T(\hat{n}_\uparrow(\tau_1) - \alpha_\uparrow^1) \cdots (\hat{n}_\downarrow(\tau_n) - \alpha_\downarrow^n) O(\tau) \rangle_0}{\langle T(\hat{n}_\uparrow(\tau_1) - \alpha_\uparrow^1) \cdots (\hat{n}_\downarrow(\tau_n) - \alpha_\downarrow^n) \rangle_0}. \qquad (29)$$

Both the numerator and the denominator of the above Eq. (29) can be written as determinants of matrices using Wick's theorem. Equation (28) is the central relation of the CTQMC algorithm because starting from this equation, the Metropolis-Hastings algorithm can be employed to generate a Markov chain of configurations C_n. At this point, we have to interpret $(\frac{U}{2})^n \det \mathbf{M}_{C_n}$ as the statistical weight of a given configuration C_n that, in general, is impossible, as $\det \mathbf{M}_{C_n}$ is a complex number. Therefore, we have to replace $(\frac{U}{2})^n \det \mathbf{M}_{C_n}$ by its modulus and account for the phase in the measurement of the observables. Fortunately, in the present case, the statistical weights are always real and nonnegative so that we can simply calculate the contribution to the observable $O(\tau)$ for a given configuration C_n in the Markov chain as $\langle\langle O(\tau) \rangle\rangle_{C_n}$.

B. Wick's theorem for each configuration

For the measurement of higher Green's functions of the form $\langle T\gamma_1^\dagger \gamma_{1'} \cdots \gamma_m^\dagger \gamma_{m'} \rangle$, where $\gamma_i^\dagger$ stands for $d_{\sigma_i}^\dagger(\tau_{i,\mathrm{meas}})$ or $c_{k_i,\sigma_i,\alpha_i}^\dagger(\tau_{i,\mathrm{meas}})$ depending on the quantity of interest, the calculation of the contribution $\langle\langle T\gamma_1^\dagger \gamma_{1'} \cdots \gamma_m^\dagger \gamma_{m'} \rangle\rangle_{C_n}$ is tedious and time consuming. Luckily for every configuration C_n a relation similar to Wick's theorem can be found, which greatly simplifies the calculation of higher Green's functions. It is closely connected to the determinant identity [Eq. (A2)] proven in the Appendix. The application of the ordinary Wick's theorem to the denominator and the numerator of Eq. (29) yields

$$\langle\langle T\gamma_1^\dagger \gamma_{1'} \cdots \gamma_m^\dagger \gamma_{m'} \rangle\rangle_{C_n} = \frac{\det \mathbf{B}_{C_n}}{\det \mathbf{M}_{C_n}}, \qquad (30)$$

where we have defined the matrix $\mathbf{B}_{C_n} \in \mathbb{C}^{(2n+m) \times (2n+m)}$ as

$$\mathbf{B}_{C_n} = \begin{pmatrix} & & & \langle T\gamma_1^\dagger \mathbf{d}(\tau_1) \rangle_0 & \cdots & \langle T\gamma_m^\dagger \mathbf{d}(\tau_1) \rangle_0 \\ & \mathbf{M}_{C_n} & & \vdots & \ddots & \vdots \\ & & & \langle T\gamma_1^\dagger \mathbf{d}(\tau_n) \rangle_0 & \cdots & \langle T\gamma_m^\dagger \mathbf{d}(\tau_n) \rangle_0 \\ \langle T\mathbf{d}^\dagger(\tau_1) \gamma_{1'} \rangle_0 & \cdots & \langle T\mathbf{d}^\dagger(\tau_n) \gamma_{1'} \rangle_0 & \langle T\gamma_1^\dagger \gamma_{1'} \rangle_0 & \cdots & \langle T\gamma_m^\dagger \gamma_{1'} \rangle_0 \\ \vdots & \ddots & \vdots & \vdots & \ddots & \vdots \\ \langle T\mathbf{d}^\dagger(\tau_1) \gamma_{m'} \rangle_0 & \cdots & \langle T\mathbf{d}^\dagger(\tau_n) \gamma_{m'} \rangle_0 & \langle T\gamma_1^\dagger \gamma_{m'} \rangle_0 & \cdots & \langle T\gamma_m^\dagger \gamma_{m'} \rangle_0 \end{pmatrix}. \qquad (31)$$

Defining the matrices $\mathbf{B}_{C_n}^{\mathbf{ij}} \in \mathbb{C}^{(2n+1)\times(2n+1)}$, we can make use of the determinant identity [Eq. (A2)]

$$
\mathbf{B}_{C_n}^{\mathbf{ij}} = \begin{pmatrix} & & & \langle T\gamma_j^\dagger \mathbf{d}(\tau_1)\rangle_0 \\ & \mathbf{M}_{C_n} & & \vdots \\ & & & \langle T\gamma_j^\dagger \mathbf{d}(\tau_n)\rangle_0 \\ \langle T\mathbf{d}^\dagger(\tau_1)\gamma_{i'}\rangle_0 & \cdots & \langle T\mathbf{d}^\dagger(\tau_n)\gamma_{i'}\rangle_0 & \langle T\gamma_j^\dagger \gamma_{i'}\rangle_0 \end{pmatrix},
$$

(32)

yielding

$$
\frac{\det \mathbf{B}_{C_n}}{\det \mathbf{M}_{C_n}} = \frac{1}{(\det \mathbf{M}_{C_n})^n}\det\begin{pmatrix} \det \mathbf{B}_{C_n}^{\mathbf{11}} & \cdots & \det \mathbf{B}_{C_n}^{\mathbf{1m}} \\ \vdots & \ddots & \vdots \\ \det \mathbf{B}_{C_n}^{\mathbf{m1}} & \cdots & \det \mathbf{B}_{C_n}^{\mathbf{mm}} \end{pmatrix}.
$$

(33)

From Eq. (29) it is obvious that $\det \mathbf{B}_{C_n}^{\mathbf{ij}}/\det \mathbf{M}_{C_n}$ is identical to the contribution of the configuration C_n to the one-particle Green's function $\langle T\gamma_j^\dagger \gamma_{i'}\rangle$. Hence, Wick's theorem holds for every configuration C_n and is given by

$$
\langle\langle T\gamma_1^\dagger \gamma_{1'} \cdots \gamma_m^\dagger \gamma_{m'}\rangle\rangle_{C_n}
$$

$$
= \det\begin{pmatrix} \langle\langle T\gamma_1^\dagger \gamma_{1'}\rangle\rangle_{C_n} & \cdots & \langle\langle T\gamma_m^\dagger \gamma_{1'}\rangle\rangle_{C_n} \\ \vdots & \ddots & \vdots \\ \langle\langle T\gamma_1^\dagger \gamma_{m'}\rangle\rangle_{C_n} & \cdots & \langle\langle T\gamma_m^\dagger \gamma_{m'}\rangle\rangle_{C_n} \end{pmatrix}.
$$

(34)

This relation is particularly useful in a simulation measuring multiple physical observables as measurements of single-particle Green's functions can be reused in an economic way.

V. NUMERICAL RESULTS

In this section, we present the results obtained by CTQMC simulations for the model (1). We restrict ourselves to the case of half filling, $\epsilon_d = 0$ and $\mu = 0$. In the first part of this section, we will discuss the results for static quantities including the Josephson current, double occupancy, and pair correlations on the quantum dot. We then proceed to dynamical quantities such as the single-particle spectral function and the dynamical spin structure factor.

A. Josephson current

The Josephson current flowing through the Quantum dot can be calculated directly within the CTQMC method, as it is given by an equal-time Green's function,

$$
\langle j_\alpha \rangle = i\frac{V}{\sqrt{N}}\sum_{k,\sigma}\langle \tilde{c}_{k,\sigma,\alpha}^\dagger \tilde{d}_\sigma - \tilde{d}_\sigma^\dagger \tilde{c}_{k,\sigma,\alpha}\rangle.
$$

(35)

We show here our results for the Josephson current at an inverse temperature of $\beta = 50$ as a function of the superconducting gap Δ. For small values of Δ, we observe a sinusoidal form of the Josephson current as a function of the phase difference ϕ with increasing amplitude, as Δ increases (see Fig. 7).
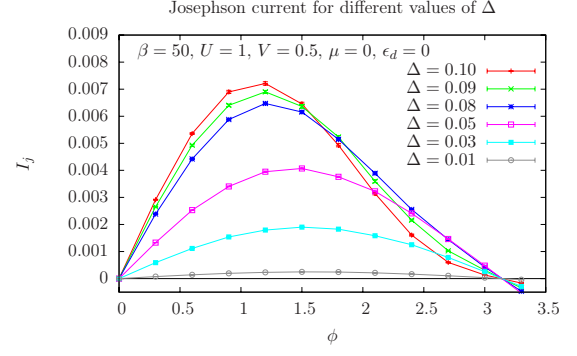

FIG. 7. (Color online) Josephson current in the 0 junction regime.

This parameter regime is known as the 0-junction regime because the Josephson current $I_j(\phi) = \frac{\partial\Omega}{\partial\phi}$ has a zero with positive slope at $\phi = 0$, corresponding to a minimum in the grand potential Ω at $\phi = 0$ (see Fig. 5 in Ref. 23).

If the value of Δ is further increased, the behavior of the Josephson current changes, as in the region $\Delta \approx 0.15\cdots0.35$ the Josephson current shows a zero between $\phi = 0$ and $\phi = \pi$. (see Fig. 8). This leads to a minimum in the grand potential at π and the parameter regime is called $0'$ or π' regime depending on which minimum of the grand potential is the global one.[34] The behavior of the Josephson current is in accordance with the behavior of the double occupancy seen in Fig. 12, as in the same parameter region, where we observe the $0'$ to π' transition, the drop of the double occupancy as a function of ϕ can be observed, which is linked to the change in the curvature of the current-phase relation of the Josephson current.

For larger values of Δ, the sign of the Josephson current changes and the grand potential shows now a single minimum at $\phi = \pi$, this regime is therefore called the π regime. (see Fig. 9).

The picture for the behavior of the grand potential as a function of ϕ that we get from the current-phase relation of the Josephson current agrees very nicely with the results presented by Benjamin et al.[35]

The current-phase relations for the different phases presented here were also extensively studied by Karrasch et al.[23] using the fRG and NRG methods, Choi et al.[16] using the NRG method, as well as by Siano and Egger[20–22] using the
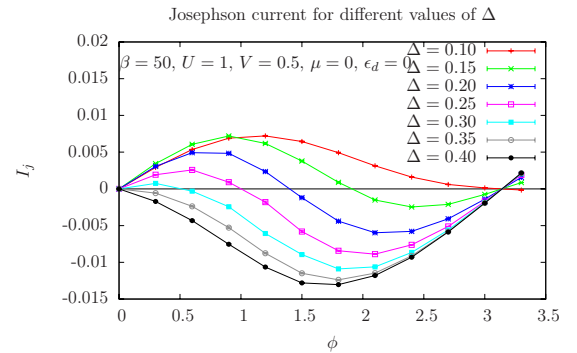

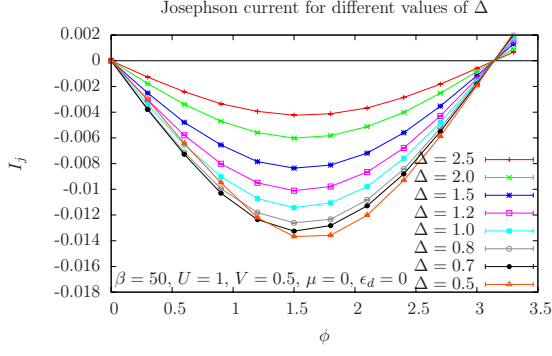FIG. 8. (Color online) Josephson current in the $0'$ and π' junction regimes.

FIG. 9. (Color online) Josephson current in the π junction regime.

Hirsch-Fye QMC method. Even though the numerical exactness of certain results has been debated, the results of all numerical works show very good qualitative agreement and are confirmed by the present results.

In the literature,[22,23] the temperature dependence of the current-phase relation of the Josephson current has been discussed. We show CTQMC results in Fig. 10 which look very similar to the Siano and Egger[22] result. As CTQMC is numerically exact, our result suggests that the crossing of all curves in one single point[23] at $I_j = 0$ found in the approximate finite temperature NRG is not universal.

B. Double occupancy

We learned from the toy model described in Sec. III that the system exhibits a phase transition from the singlet phase to the doublet phase as U is increased. This picture is consistent with the NRG results of Bauer *et al.*[18] The phase transition can be observed in the double occupancy $\langle \hat{n}_\uparrow \hat{n}_\downarrow \rangle$ of the quantum dot, which is proportional to $\frac{\partial \Omega}{\partial U}$, where Ω is the grand potential. At $T = 0$, a sharp step function of the double occupancy is expected. While the $T = 0$ regime is not directly accessible to quantum Monte Carlo calculations, we calculated the double occupancy for different temperatures using the CTQMC method. The results are shown in Fig. 11. From the data, it is obvious that with decreasing temperature the curves converge to the step function of the limit $T = 0$, which

FIG. 11. (Color online) Double occupancy $\langle \hat{n}_\uparrow \hat{n}_\downarrow \rangle$ of the quantum dot at $\Delta = 1.0$. The data show a jump in the double occupancy becoming sharper with decreasing temperature.

is a clear sign for a first-order phase transition, reflecting a level crossing of the two ground states. This is in complete accordance with the results for the toy model.

It is interesting to correlate the Josephson current as a function of the phase difference $\phi = \phi_L - \phi_R$ for various values of Δ (see Sec. V A), with the double occupancy on the dot. As depicted in Fig. 12, for very small values of Δ as well as for $\Delta \gtrsim 0.4$, we see that the double occupancy is a constant function of ϕ. This corresponds to a current-phase relation for the Josephson current fixed in either the π- or the 0-junction regime. For intermediate values of Δ, we observe a far more interesting behavior of the double occupancy: At a certain value of ϕ, the double occupancy drops to a smaller value. This drop is of course smeared out by the finite temperature but can be understood as a way to drive the phase transition from the 0- to the π-junction regime by the phase difference ϕ.

C. Pair correlation

In agreement with the NRG result of Choi *et al.*[16] as well as with the mean-field results by Salkola *et al.*,[30] we obtain the local pair correlation on the quantum dot shown in Fig. 13. For small Δ, the local pair correlation increases because of the proximity effect, as an increasing magnitude of the
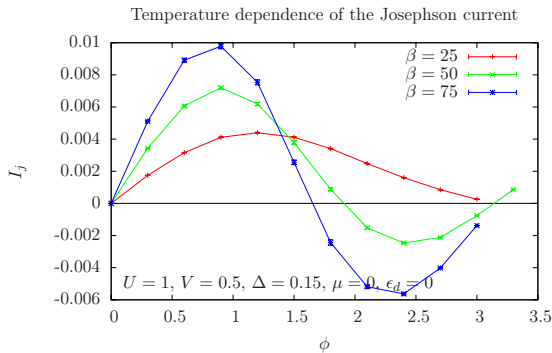

FIG. 10. (Color online) Josephson current for different temperatures $1/\beta$. The current-phase relations do not intersect at one single point as suggested by the NRG results of Karrasch *et al.* (Ref. 23).
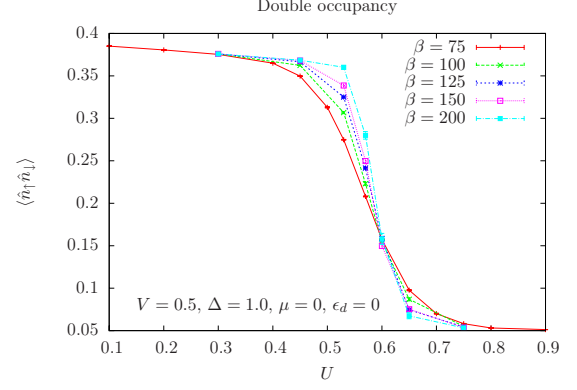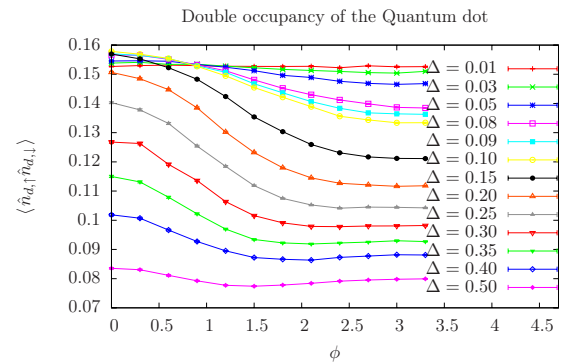

FIG. 12. (Color online) Double occupancy of the quantum dot as a function of the phase difference $\phi = \phi_L - \phi_R$ for different values of Δ.
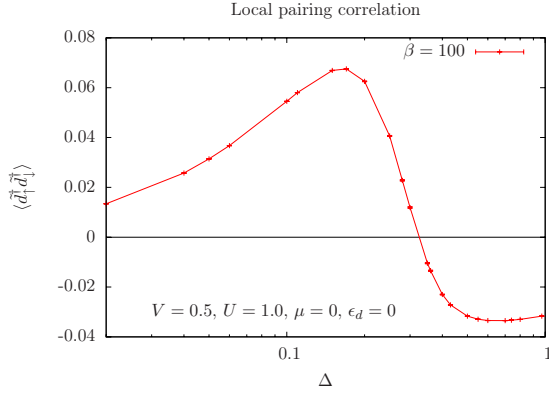
FIG. 13. (Color online) Local pair correlation $\Delta_d = \langle \tilde{d}^\dagger_\uparrow \tilde{d}^\dagger_\downarrow \rangle$ as a function of Δ. We observe the same behavior as Choi *et al.* (Ref. 16) which is also in very good agreement with the pair correlation expected for the effective model discussed in Sec. III C.

pair field Δ in the leads induces a growing pair correlation on the quantum dot. The sharp sign change at the critical value of Δ observed at zero temperature is smeared out at finite temperatures but the qualitative behavior is exactly the same as for the effective model discussed in Sec. III C. We therefore conclude that the sign change in the pair correlation is due to residual pairing on the quantum dot in the doublet phase which decreases with Δ.

The same qualitative behavior of the local pair correlation is also observed, if U is changed instead of Δ as discussed in Refs. 18 and 30. The sign change in the local pair correlation Δ_d is traditionally expressed as a π-phase shift in Δ_d.

D. Spectral function

All quantities studied so far suggest that a first-order phase transition occurs when we tune the system from the 0-junction to the π-junction regime. This can be confirmed by studying dynamical quantities such as the spectral function.

In Fig. 14 we show the spectral function $A(\omega)$ of the quantum dot as a function of Δ. The data have been calculated from the CTQMC data for the Green's function $G_{dd}^{\uparrow\uparrow}(\tau)$ using stochastic analytic continuation.[36,37] This method works especially well for the low-energy spectrum and sharp excitations while the high-energy spectrum and excitation continua are more difficult to resolve. Inside the gap, the formation of Andreev bound states can be seen very well.

In the region of $\Delta \approx 0$ we see the Kondo resonance. As a function of growing values of Δ and as a consequence of the opening of the quasiparticle gap at the Fermi level, the Kondo resonance evolves to the Andreev bound state. Note that at the mean-field level, the Kondo resonance merely corresponds to a virtual bound state. Opening a quasiparticle gap at the Fermi level drives the lifetime of this virtual bound state to infinity. In the parameter region which corresponds to the 0-junction regime of the Josephson current ($\Delta \approx 0 \cdots 0.1$), we observe Andreev bound states with excitation energies approaching $\omega = 0$. This corresponds to the crossing point in Fig. 14 and has also been observed by Bauer *et al.* for fixed Δ and increasing U in Ref. 18.
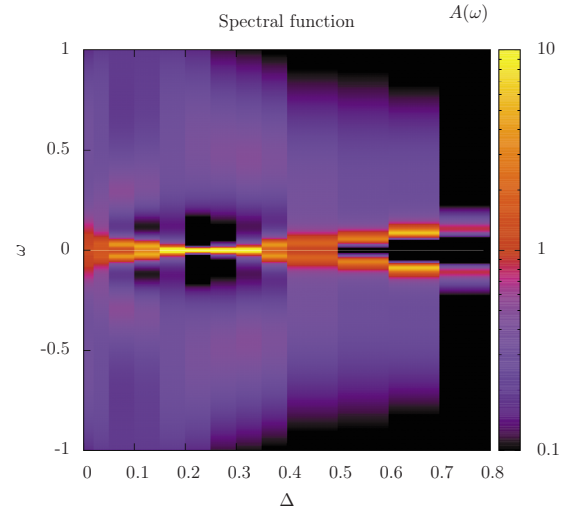

FIG. 14. (Color online) Spectral function $A(\omega)$ as a function of Δ for the parameters $\beta = 100$, $U = 1.0$, and $V = 0.5$ at half filling and zero phase difference between the two superconductors.

The comparison of the quantum Monte Carlo data shown in Fig. 14 with the result obtained from the effective model discussed in Sec. III D is particularly insightful. The spectral signature is very similar except for the lack of the Kondo resonance due to the finite size of the effective model. In the effective model, the Andreev bound-state excitation corresponds to the energy difference between the ground states of the singlet and the doublet phases. The position Δ at which the Andreev bound states cross at $\omega = 0$ has been identified as a clear sign for the crossing of the ground states of the singlet and doublet phases. Hence, we interpret the crossing of the Andreev bound states in the CTQMC data as a very strong sign for a level crossing and hence a first-order phase transition from the singlet to the doublet phases in the full model.

E. Dynamical spin structure factor

In addition to the spectral function, the dynamical spin structure factor $S(\omega)$ defined in Eq. (22) provides a way of characterizing the phases of the system. For $\Delta = 0$, we clearly see a suppressed spectral weight at $\omega = 0$ and a peak which corresponds to the characteristic energy scale of the Kondo temperature T_K. From the peak position, we obtain a rough estimate for the Kondo temperature of $T_K \approx 0.06$.

From $\Delta \approx 0.05$ onward, spectral weight is accumulated at $\omega = 0$ ultimately forming a pronounced sharp local-moment peak for large values of Δ. As the Kondo temperature is a measure for the energy required to break the Kondo singlet, we expect the Kondo effect to break down at a value of $\Delta \approx T_K$. This is indeed observed in Fig. 15.

The signature of the breakdown of the Kondo resonance also shows up in the spectral function plotted in Fig. 14. Since the Kondo resonance stems from a screening of the magnetic moment by conduction electrons in an energy window T_K around the Fermi level, the opening of a single-particle gap of order T_K destroys the Kondo resonance giving way to an Andreev bound state.
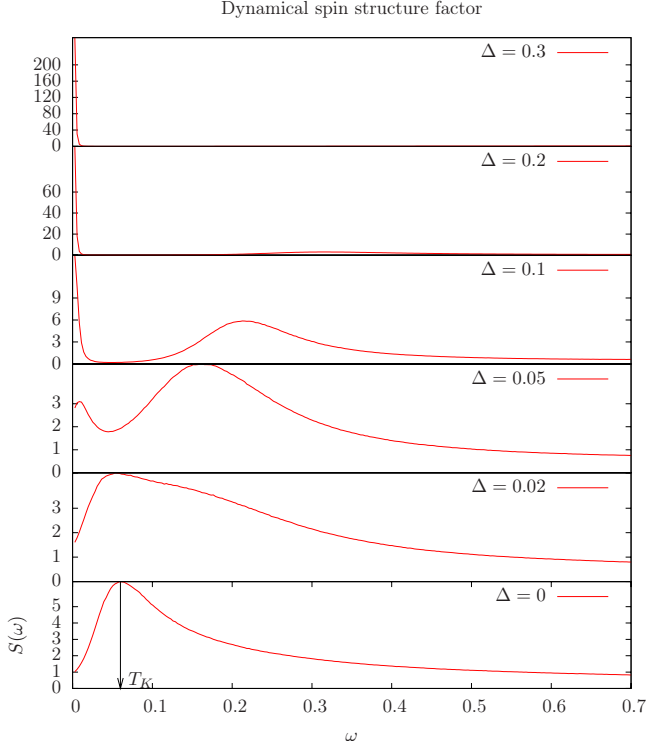
FIG. 15. (Color online) Dynamical spin structure factor $S(\omega)$ as a function of Δ for the parameters $\beta = 100$, $U = 1.0$, and $V = 0.5$ at half filling and zero phase difference between the two superconductors. For $\Delta = 0$ we can roughly estimate the Kondo temperature $T_K \approx 0.06$ from the peak position of $S(\omega)$.

The breakdown of the Kondo resonance is accompanied by a change in the curvature in the current-phase relation of the Josephson current which is a precursor for the transition to the $0'$ phase (see the curves for $\Delta = 0.05$ and 0.08 in Fig. 7). We also observe that after the transition from the π' to the π regime has occurred (see the current-phase relation of the Josephson current of Fig. 8) the peak at finite ω vanishes and all the spectral weight is accumulated in the very sharp local-moment peak at $\omega = 0$.

F. Charge gap

From the dynamical charge structure factor, we can determine the gap Δ_c to local charge fluctuations on the dot with two different methods.[38] One way to extract the charge gap is to read off the peak position of the lowest lying excitation in the dynamical charge structure factor obtained from the charge correlation function $C_c(\tau) = \langle \tilde{n}(\tau)\tilde{n} \rangle - \langle \tilde{n} \rangle \langle \tilde{n} \rangle$ via stochastic analytic continuation. The other way of extracting the charge gap from $C_c(\tau)$ is based on the fact that the charge structure factor $N(\omega)$ is linked to $C_c(\tau)$ via

$$C_c(\tau) \propto \int_{-\infty}^{\infty} d\omega\, e^{-\tau\omega} N(\omega). \tag{36}$$

If $N(\omega)$ is sharply peaked around a certain value ω_p, we can approximate $N(\omega)$ by $N(\omega) \approx \delta(\omega - \omega_p)$. This corresponds to $C_c(\tau) \approx e^{-\tau\omega_p}$. Therefore, a least-squares fit of an exponential
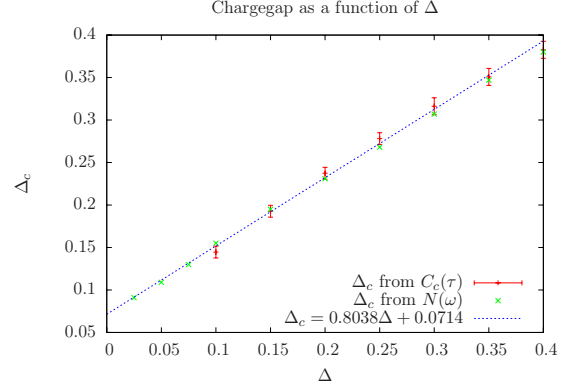

FIG. 16. (Color online) Charge gap Δ_c as a function of Δ. We calculated the dynamical charge structure factor from the charge-charge correlation function $C_c(\tau)$ using stochastic analytic continuation and extracted the charge gap using two different methods. First, we read off the charge gap directly from the stochastic analytic continuation data and second, we calculated the charge gap from the charge-charge correlation function. The straight line is a linear fit through the numerical data.

function $e^{-\tau\omega_p}$ to $C_c(\tau)$ in a region where only one single mode dominates can reveal the frequency ω_p at which $N(\omega)$ is peaked. The applicability of the method can be seen in the half logarithmic plot of $C_c(\tau)$, where a sharply peaked charge structure factor $N(\omega)$ is reflected by a region in which $C_c(\tau)$ can be well approximated by a straight line.

The data obtained using these methods are shown in Fig. 16. In the context of the effective model discussed in Sec. III F, we observe that the behavior of the charge gap of the full model clearly differs from that of the effective model. Especially, we do not see any signature of the phase transition in the behavior of the charge gap.

The charge gap opens approximately linearly with Δ. It is very hard to extract the charge gap from the numerical data at small Δ, therefore we can only extrapolate to $\Delta = 0$. Here, it appears that we have a finite charge gap even in the absence of superconductivity. The fact that the local charge fluctuations remain gaped confirms the picture that the 0 to π transition occurs only in the spin sector.

VI. DMFT

A. Periodic Anderson model with BCS conduction band

In the previous sections, we have studied the first-order phase transition in the impurity model (1). As the DMFT provides a link between impurity models and lattice models, we can ask the question if the singlet to doublet-phase transition observed in the impurity model is also realized in a corresponding lattice model.

An appropriate lattice model will of course include a U(1) symmetry-breaking term like the impurity model (1) does and in fact in the framework of the DMFT, a periodic Anderson model extended by the BCS mean-field Hamiltonian (BCS-PAM) for the conduction-band electrons corresponds to the impurity model presented in the previous sections.[39] The Hamiltonian of the BCS-PAM is given by

$$H = H_c + H_f + H_V \tag{37}$$

with

$$H_c = \sum_{k,\sigma} \xi(k) \tilde{c}^\dagger_{k,\sigma} \tilde{c}_{k,\sigma} - \Delta \sum_k (\tilde{c}^\dagger_{k,\uparrow} \tilde{c}^\dagger_{-k\downarrow} + \text{H.c.}), \tag{38}$$

$$H_f = \sum_{k,\sigma} \xi_f \tilde{f}^\dagger_{k,\sigma} \tilde{f}_{k,\sigma} + U \sum_{i_f} \left(\tilde{n}_{i_f,\uparrow} - \frac{1}{2} \right) \left(\tilde{n}_{i_f,\downarrow} - \frac{1}{2} \right), \tag{39}$$

$$H_V = -V \sum_{k,\sigma} (\tilde{c}^\dagger_{k,\sigma} \tilde{f}_{k,\sigma} + \text{H.c.}). \tag{40}$$

We have considered a square lattice with hopping matrix element t between the conduction electrons such that

$$\xi(k) = -2t[\cos(ka_x) + \cos(ka_y)]. \tag{41}$$

Note that the impurity model (1) has a large range of applications in the DMFT ranging from the attractive Hubbard model with U(1) symmetry broken solutions studied in Refs. 40 and 41 to the BCS-PAM, which is considered here.

The treatment of this model within DMFT involves the same steps as for the impurity model (1), introducing a particle-hole transformation for the spin-down operators. The Hamiltonian can then be cast in the form $H = H_0 + H_U$ with

$$H_0 = \sum_k \mathbf{c}^\dagger_k \mathbf{E}(k) \mathbf{c}_k - V \sum_k (\mathbf{c}^\dagger_k \sigma_z \mathbf{f}_k + \text{H.c.}) + \sum_k \mathbf{f}^\dagger_k \epsilon_f \mathbf{f}_k \tag{42}$$

and $H_U = -U \Sigma_{i_f} (n_{i_f,\uparrow} - \frac{1}{2})(n_{i_f,\downarrow} - \frac{1}{2})$. Here, we have used the same Nambu-spinor notation as in Sec. II with the exception that d operators have been renamed f to be consistent with the literature.[29,32]

B. DMFT with superconducting medium

The standard DMFT can be easily adapted to a superconducting bath using the Nambu formalism.[29] We obtain the self-consistency equation for a finite lattice with N sites expressed by a 2×2 matrix equation,

$$\mathbf{G}^{\text{ff}}(i\omega_n) = \frac{1}{N} \sum_\mathbf{k} [\mathbf{G}^{0,\text{ff}^{-1}}_{\mathbf{kk}}(i\omega_n) - \mathbf{\Sigma}^{\text{ff}}(i\omega_n)]^{-1}. \tag{43}$$

Here, $\mathbf{G}^{\text{ff}}(i\omega_n) = -\int_0^\beta d\tau e^{-i\omega_n\tau} \langle Tf(\tau)\mathbf{f}^\dagger \rangle$ is the full Matsubara Green's function of the reference model, $\mathbf{G}^{0,\text{ff}}_{\mathbf{kk}}(i\omega_n)$ is the Matsubara f Green's function of the bare lattice model, and $\mathbf{\Sigma}^{\text{ff}}$ is the self-energy. Equation (43) can be solved by iteration starting usually at a self-energy $\mathbf{\Sigma}^{\text{ff}} \equiv 0$. From $\mathbf{G}^{\text{ff}}(i\omega_n)$, the bare Green's function $\mathcal{G}^{\text{ff}}_0(i\omega_n)$ of the reference model can be calculated using Dyson's equation $\mathcal{G}^{\text{ff}^{-1}}_0 = \mathbf{G}^{\text{ff}^{-1}} + \mathbf{\Sigma}^{\text{ff}}$. The reference model, which is now described by $\mathcal{G}^{\text{ff}}_0$ and the interaction part of the Hamiltonian can subsequently be solved using the CTQMC method yielding $\mathbf{G}^{\text{ff}}(i\omega_n)$ for the next DMFT iteration.

C. Hysteresis

In the DMFT, we can calculate the double occupancy $\langle \tilde{f}^\dagger_{\uparrow,i} \tilde{f}_{\uparrow,i} \tilde{f}^\dagger_{\downarrow,i} \tilde{f}_{\downarrow,i} \rangle$ of the f sites, which is together with the as-
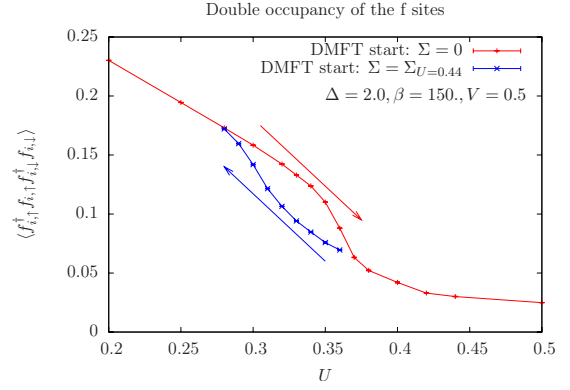

FIG. 17. (Color online) Double occupancy of the f sites in the BCS-PAM. In the proximity of the critical value of U, we observe two different solutions of the DMFT self-consistency cycle. The upper (thin/red) branch is generated, if we start the DMFT algorithm with a self-energy $\Sigma \equiv 0$ while we obtain the solution shown by the lower (thick/blue) branch if we take the self-energy of the data point at $U = 0.44$ as the starting point of the DMFT iterations.

sumption of a homogeneous system proportional to $\frac{\partial\Omega}{\partial U}$. Therefore, we expect a jump in the double occupancy to appear at a critical value of U, if we have a first-order phase transition as in the impurity problem.

Figure 17 shows our result for the double occupancy of the f sites as a function of U. Depending on the initial choice of the self-energy in the DMFT cycle, we obtain two different solutions. If we start with the local Green's function of the bare lattice model, which corresponds to a self-energy $\mathbf{\Sigma} \equiv 0$, we obtain the upper branch of the hysteresis. The lower branch is obtained by taking the self-energy of the solution in the strong-coupling phase at $U = 0.44$ as starting point for the DMFT cycle. The coexistence of two solutions is a strong hint that a first-order phase transition occurs.

It should be noted that beginning at a value of $U \approx 0.34$, the upper branch of the hysteresis becomes unstable, i.e., the inherent fluctuations of the Monte Carlo results suffice to drop from the upper branch of the hysteresis to the lower branch after a certain number of iterations. Increasing the number of Monte Carlo measurements delays the drop to the lower branch to a higher number of iterations. This behavior can be understood in the following way: in the coexistence region, the grand potential Ω of the upper and lower branches of the hysteresis cross at a certain value of U. For small values of U, Ω is minimal on the upper branch while the lower branch is metastable and for larger values of U, however, the stable solution is the lower branch.

In the strong-coupling phase and on the lower branch of the hysteresis, the Monte Carlo results suddenly develop a finite magnetization corresponding to a frozen spin. This is due to divergent autocorrelation times in the Monte Carlo simulation and is linked to the physical formation of a local moment.

D. Local dynamical spin structure factor

To further classify the weak and strong-coupling phases, we calculate the local dynamical spin structure factor $S(\omega)$
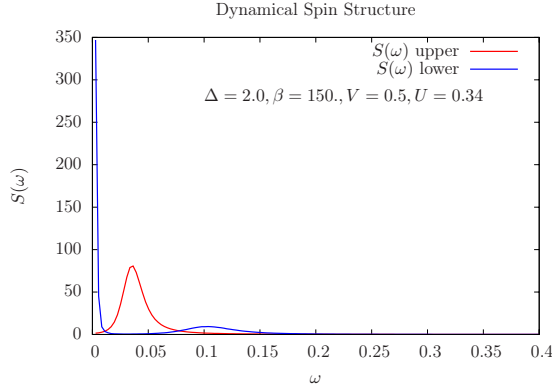
FIG. 18. (Color online) Dynamical spin structure factor for the upper and the lower branches of the hysteresis in Fig. 17. Clearly, the upper branch of the hysteresis corresponds to a singlet solution while the lower branch shows a local moment.

$= \frac{1}{N}\Sigma_{\mathbf{q}} S(\mathbf{q},\omega)$. The Lehmann representation for $S(\omega)$ is given by Eq. (22), where in this case $S_+ = S_+^{f,i}$.

As in the impurity case, $S(\omega)$ is a measure for the energy needed to flip the spin on an f site. Figure 18 shows the result for the local dynamical spin structure factor on both branches of the hysteresis. The solution corresponding to the upper branch of the hysteresis is linked to the weak-coupling regime and shows a characteristic energy scale required for flipping a spin.

The lower branch of the hysteresis represents the strong-coupling phase and shows a clear local-moment peak in the dynamical spin structure factor at $\omega=0$. This behavior reflects exactly the single impurity physics discussed in the previous section where we observed the Kondo effect in the weak-coupling phase and the formation of a local moment in the strong-coupling phase.

E. f density of states

In order to investigate the behavior of the f bands at the phase boundary and to be able to compare with the single impurity model, we calculate the density of states for the f sites ρ_{ff} directly from the local Green's function $G(\tau)$ using the stochastic analytic continuation method for different values of U. From Fig. 19, one can recognize the signature of
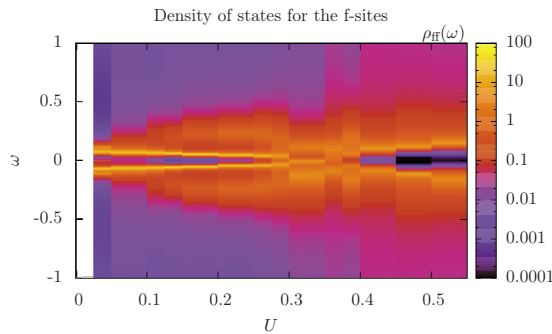

FIG. 19. (Color online) Density of states for the f electrons as a function of U for the parameters $V=0.5$, $\Delta=2$, $\mu=\epsilon_f=0$, and $\beta=100$.
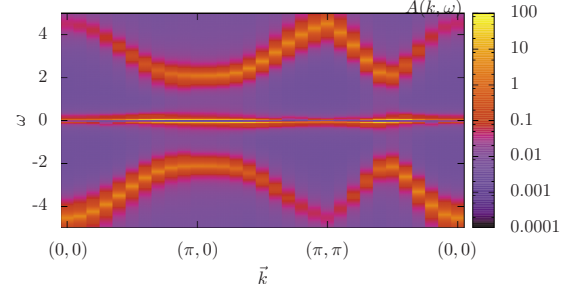

FIG. 20. (Color online) Trace of the spectral function $A(\mathbf{k},\omega)$ at $\beta=100$ in the singlet regime. The parameters of the simulation were given by $U=0.125$, $V=0.5$, $\Delta=2$, and $\mu=\epsilon_f=0$.

the impurity physics (see Sec. V D), namely, the crossing of Andreev bound states in the vicinity of the first-order transition at $U\approx 0.35$. Note that we have only shown the level crossing for the impurity model if Δ is changed but for varying U, the crossing of the Andreev bound states in the impurity model (1) has been observed by Bauer *et al.*[18] Clearly in the lattice model, one expects the Andreev bound states to acquire a dispersion relation which shows up as a finite width in ρ_{ff}.

F. Dispersion relation of Andreev bound states

We have seen in the previous sections that the local physics of the single impurity model can be carried over to the lattice case within the DMFT approximation. Here, we concentrate on unique features of the lattice model (37), namely, the dispersion relation of the f bands as obtained by analyzing the single-particle spectral function.

Using the local self-energy of the DMFT, $\mathbf{\Sigma}^{\mathrm{ff}}(i\omega_n)$, this quantity is extracted from the Green's functions

$$\mathbf{G}_{\mathbf{kk}}^{\mathrm{ff}}(i\omega_n) = [\mathbf{G}_{\mathbf{kk}}^{0,\mathrm{ff}}(i\omega_n)^{-1} - \mathbf{\Sigma}^{\mathrm{ff}}(i\omega_n)]^{-1} \quad (44)$$

and

$$\mathbf{G}_{\mathbf{kk}}^{\mathrm{cc}}(i\omega_n) = \mathbf{G}_{\mathbf{kk}}^{0,\mathrm{cc}}(i\omega_n) - \mathbf{G}_{\mathbf{kk}}^{0,\mathrm{cf}}(i\omega_n)\mathbf{G}_{\mathbf{kk}}^{\mathrm{ff}}(i\omega_n)\mathbf{G}_{\mathbf{kk}}^{0,\mathrm{fc}}(i\omega_n), \quad (45)$$

where $\mathbf{G}_{\mathbf{kk}}^{0,\mathrm{cc}}(i\omega_n)$, $\mathbf{G}_{\mathbf{kk}}^{0,\mathrm{ff}}(i\omega_n)$, $\mathbf{G}_{\mathbf{kk}}^{0,\mathrm{cf}}(i\omega_n)$, and $\mathbf{G}_{\mathbf{kk}}^{0,\mathrm{fc}}(i\omega_n)$ denote the noninteracting Green's functions for the corresponding orbitals in the unit cell.

Using the stochastic analytic continuation, these Green's functions can be rotated to real frequencies, yielding, in principle, the spectral function $\mathbf{A}(\mathbf{k},\omega)$. For each $\mathbf{k}$ point and real frequency this quantity is a 4×4 matrix since we have a 2×2 Nambu spectral function for each combination of f and c orbitals in the unit cell. Our analysis of the spectral function is based on the basis independent quantity $A(\mathbf{k},\omega)=\mathrm{Tr}\,\mathbf{A}(\mathbf{k},\omega)$.

Figure 20 plots this quantity in the singlet phase. The overall structure of the spectral function is similar to the structure observed for the bare BCS-PAM characterized by the four bands,
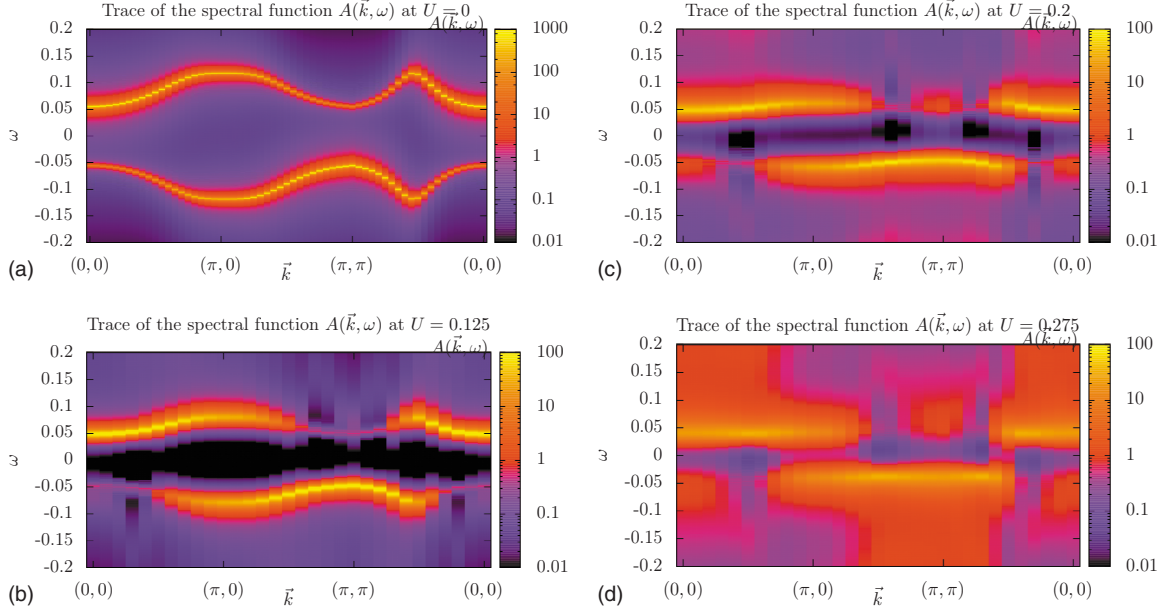
FIG. 21. (Color online) Trace of the spectral function $A(\mathbf{k}, \omega)$ at $\beta = 100$ in the singlet regime for increasing interaction U. The width of the f bands clearly decreases and the dispersion becomes weaker. The parameters of the simulations were given by $V = 0.5$, $\Delta = 2$, and $\mu = \epsilon_f = 0$.

$$E_{\pm,\pm}(\mathbf{k}) = \pm \sqrt{V^2 + E^2(\mathbf{k})/2 \pm E(\mathbf{k}) \sqrt{V^2 + E^2(\mathbf{k})/4}}, \tag{46}$$

where $E(\mathbf{k}) = \sqrt{\epsilon^2(\mathbf{k}) + \Delta^2}$. The bands with dominant c character, $E_{\pm}^c(\mathbf{k}) \equiv E_{\pm,+}(\mathbf{k})$, at high frequencies are well separated from the bands of dominant f character at low frequencies, $E_{\pm}^f(\mathbf{k}) = E_{\pm,-}(\mathbf{k})$. For the considered bare parameters, V is the smallest scale and sets the magnitude of the dispersion relation of the f band. In particular, expanding in V gives

$$E_{\pm}^f(\mathbf{k}) = \pm \frac{V^2}{E(\mathbf{k})} + \mathcal{O}\left(\frac{V^4}{E(\mathbf{k})^3}\right). \tag{47}$$

Starting from the point of view of the impurity model, which as seen above accounts very well for overall form of the k-integrated f-spectral function, $E_{\pm}^f(\mathbf{k})$ may be perceived as the dispersion relation of the Andreev bound states.

The singlet phase is continuously connected to the $U = 0$ point. Starting from this limit, we can account for the Hubbard U within a slave-boson approximation[42] which will renormalize the hybridization matrix element to lower values. Owing to Eq. (47) this suppresses the dispersion relation of the f electrons. This aspect is clearly observed in Fig. 21.

In the doublet phase, $U > U_c$, the paramagnetic slave-boson mean-field approach fails. In this state, the f spin is frozen and in the DMFT cycle we have imposed spin-symmetric baths thereby inhibiting magnetic ordering. The QMC data of Fig. 22 points to a very incoherent f spectral function. It is therefore tempting to model this state in terms of spin disorder: the spin of the f electrons on each site is static and points in a random direction. To provide some support for this picture we stay in the dynamical mean-field framework but consider a mean-field decomposition of the Hubbard term in the action of the impurity problem,

$$U\left(\tilde{n}_{f,\uparrow} - \frac{1}{2}\right)\left(\tilde{n}_{\downarrow} - \frac{1}{2}\right) \rightarrow -\frac{Um_z}{2}(\tilde{n}_{f,\uparrow} - \tilde{n}_{f,\downarrow}). \tag{48}$$

This mean-field approximation, accounts for the local-moment formation with z component of spin m_z. The corresponding mean-field action of the impurity model now reads
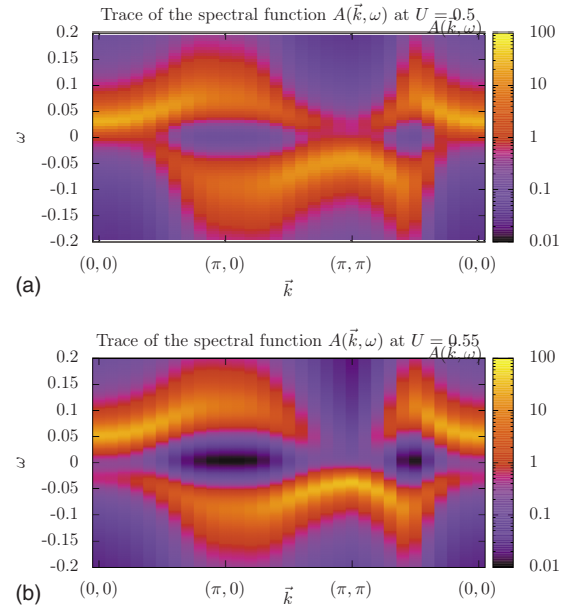

FIG. 22. (Color online) Trace of the spectral function $A(\mathbf{k}, \omega)$ at $\beta = 100$ in the doublet regime for different values of U. Here, we only show the f bands. The parameters of the simulation were given by $V = 0.5$, $\Delta = 2$, and $\mu = \epsilon_f = 0$.

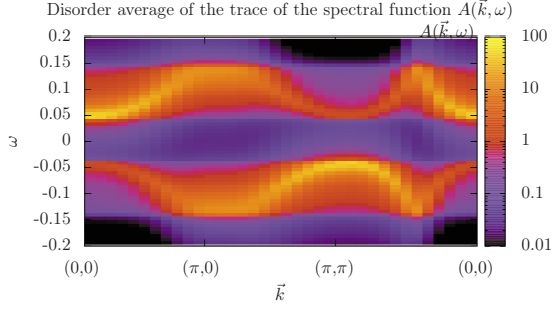Disorder average of the trace of the spectral function $A(\vec{k}, \omega)$

FIG. 23. (Color online) Trace of the spectral function $A(\mathbf{k}, \omega)$ as obtained from using Eq. (49) for the impurity action. The z component of the local moment is sampled from the box distribution $m_z \in [-M_z, M_z]$. The parameters used for this plot were given by $V = 0.5$, $U = 0.5$, $\Delta = 2$, and $M_z = 0.0375$. Here, the calculations are carried out on the real time axis such that no analytical continuation is required.

$$S_{MF} = \int_0^\beta d\tau \int_0^\beta d\tau' \widetilde{\mathbf{f}}^\dagger(\tau) \mathcal{G}^{-1}(\tau - \tau') \widetilde{\mathbf{f}}(\tau')$$
$$- \frac{U m_z}{2} \int_0^\beta d\tau \widetilde{\mathbf{f}}^\dagger(\tau) \widetilde{\mathbf{f}}(\tau), \quad (49)$$

where $\widetilde{\mathbf{f}}^\dagger = (\widetilde{f}_\uparrow^\dagger, \widetilde{f}_\downarrow)$ and $\mathcal{G}(\tau - \tau')$ corresponds to the bath Green's function. To account for disorder, the z component of the f spin is sampled from the box distribution $m_z \in [-M_z, M_z]$. Averaging over disorder at each iteration in the DMFT cycle yields the spectral function shown in Fig. 23. As apparent, the disorder average generates a finite lifetime.

VII. CONCLUSION

We have shown that the weak-coupling CTQMC algorithm is an extremely powerful unbiased tool to compute thermodynamic as well as dynamical quantities of impurity models in superconducting environments. The method can cope very well with a complex phase of the superconducting order parameter thereby allowing for the calculation of the Josephson current. Our detailed results for the impurity problem confirm the picture of a first-order phase transition between a single state and doublet state. It is accompanied by a π phase shift in the Josephson current.

Within DMFT, the physics of the BCS-PAM is mapped onto the single impurity Anderson model supplemented by a self-consistency loop. We have shown that within this approximation, the physics of the impurity model can be carried over to the lattice. In particular, at fixed superconducting order parameter Δ the first-order transition between a singlet and local-moment state as a function of growing values of U shows up in a hysteresis behavior of the double occupancy. Furthermore, the low-energy features of the local f spectral function are reminiscent of the Andreev bound states with vanishing excitation energy (i.e., a crossing point) at the critical coupling. Within the DMFT approximation, we can look into the single-particle spectral function. In the singlet phase, the low-energy features can be interpreted in terms of a dispersion relation of Andreev bound states. This state is

continuously linked to the $U = 0$ limit. In the doublet state or local-moment regime, the low-energy features of the spectral functions are incoherent. We propose to understand this in terms of models of disorder. In particular, in this state, the spin dynamics of the f electron is frozen and since we are considering paramagnetic states it points in a random different direction in each unit cell. A simple model of disorder following this picture accounts very well for the observed incoherent spectral function.

APPENDIX: PROOF OF THE DETERMINANT IDENTITY

In this section a general determinant identity is proven, which can be used to derive Wick's theorem for contributions of a configuration C_n to physical observables. Let us define the vectors $\mathbf{u_i}, \mathbf{v_i} \in \mathbb{C}^m$ and the numbers $\alpha_{ij} \in \mathbb{C}$. Further, let $A \in \mathbb{C}^{m \times m}$ be a matrix of rank m. We define the nonsingular matrices $\mathbf{M_n} \in \mathbb{C}^{(m+n) \times (m+n)}$ and $\mathbf{A_{ij}} \in \mathbb{C}^{(m+1) \times (m+1)}$ by

$$\mathbf{M_n} = \begin{pmatrix} \mathbf{A} & \mathbf{u_1} & \cdots & \mathbf{u_n} \\ \mathbf{v_1^T} & \alpha_{11} & \cdots & \alpha_{1n} \\ \vdots & \vdots & \ddots & \vdots \\ \mathbf{v_n^T} & \alpha_{n1} & \cdots & \alpha_{nn} \end{pmatrix}, \quad \mathbf{A_{ij}} = \begin{pmatrix} \mathbf{A} & \mathbf{u_j} \\ \mathbf{v_i^T} & \alpha_{ij} \end{pmatrix}. \quad (A1)$$

With these definitions, the following determinant identity holds

$$\det \mathbf{M_n} (\det \mathbf{A})^{n-1} = \det \begin{pmatrix} \det \mathbf{A_{11}} & \cdots & \det \mathbf{A_{1n}} \\ \vdots & \ddots & \vdots \\ \det \mathbf{A_{n1}} & \cdots & \det \mathbf{A_{nn}} \end{pmatrix}. \quad (A2)$$

The identity can be proven by induction in n. It is trivial for $n = 1$, so we have to start with $n = 2$, where we have to show

$$\frac{\det \mathbf{M_2}}{\det \mathbf{A}} = \frac{\det \mathbf{A_{11}}}{\det \mathbf{A}} \frac{\det \mathbf{A_{22}}}{\det \mathbf{A}} - \frac{\det \mathbf{A_{12}}}{\det \mathbf{A}} \frac{\det \mathbf{A_{21}}}{\det \mathbf{A}}. \quad (A3)$$

For the following calculations, we introduce several vectors:

$$\mathbf{u_{ij}^1} = \begin{pmatrix} \mathbf{u_j} \\ \alpha_{ij} - 1 \end{pmatrix}, \quad \mathbf{v_{ij}^2} = \begin{pmatrix} \mathbf{v_i} \\ 0 \end{pmatrix}, \quad \mathbf{u^2} = \mathbf{v^1} = \begin{pmatrix} 0 \\ 1 \end{pmatrix} \in \mathbb{C}^{m+1},$$

$$(A4)$$

$$\mathbf{u_M^1} = \begin{pmatrix} \mathbf{u_2} \\ \alpha_{12} \\ \alpha_{22} - 1 \end{pmatrix}, \quad \mathbf{v_M^2} = \begin{pmatrix} \mathbf{v_2} \\ \alpha_{21} \\ 0 \end{pmatrix}, \quad \mathbf{u_M^2} = \mathbf{v_M^1} = \begin{pmatrix} 0 \\ 1 \end{pmatrix} \in \mathbb{C}^{m+2}.$$

$$(\text{A5})$$

Let us define the *expanded* matrix $\mathbf{C}_{\text{ex}}$ of a square matrix $\mathbf{C}$ as the matrix C expanded by one row and one column containing a unit vector,

$$\mathbf{C}_{\text{ex}} = \begin{pmatrix} \mathbf{C} & 0 \\ 0^T & 1 \end{pmatrix}. \quad (\text{A6})$$

As a last definition, we introduce the abbreviation $b_{ij} = \mathbf{v}_i^T \mathbf{A}^{-1} \mathbf{u}_j$. Using these notations, we can write the matrices $\mathbf{A_{ij}}$ as

$$\mathbf{A_{ij}} = \mathbf{A}_{\text{ex}} + \mathbf{u_{ij}^1} \mathbf{v^{1}}^T + \mathbf{u^2} \mathbf{v_{ij}^{2}}^T. \quad (\text{A7})$$

To calculate the determinant $\det \mathbf{A_{ij}}$, we use the matrix determinant lemma $\det(\mathbf{A} + \mathbf{u}\mathbf{v}^T) = (1 + \mathbf{v}^T \mathbf{A}^{-1} \mathbf{u}) \det \mathbf{A}$, yielding

$$\frac{\det \mathbf{A_{ij}}}{\det \mathbf{A}_{\text{ex}}} = \left[1 + \mathbf{v_{ij}^{2}}^T (\mathbf{A}_{\text{ex}} + \mathbf{u_{ij}^1} \mathbf{v^{1}}^T)^{-1} \mathbf{u^2} \right] (1 + \mathbf{v^{1}}^T \mathbf{A}_{\text{ex}}^{-1} \mathbf{u_{ij}^1}).$$

$$(\text{A8})$$

The inverse matrix of $(\mathbf{A}_{\text{ex}} + \mathbf{u_{ij}^1} \mathbf{v^{1}}^T)$ can be obtained from the Sherman-Morrison formula and a tedious calculation making use of the special form of the vectors and matrices gives the result

$$\frac{\det \mathbf{A_{ij}}}{\det \mathbf{A}} = \alpha_{ij} - b_{ij}. \quad (\text{A9})$$

From this, the right-hand side of Eq. (A3) can be easily obtained. For the left-hand side, we have to perform an analogous calculation using the decomposition of the matrix $\mathbf{M_2}$,

$$\mathbf{M_2} = \mathbf{A_{11}}_{\text{ex}} + \mathbf{u_M^1} \mathbf{v_M^{1}}^T + \mathbf{u_M^2} \mathbf{v_M^{2}}^T. \quad (\text{A10})$$

Again, we apply the matrix determinant lemma two times and insert the Sherman-Morrison formula to calculate the inverse matrix of $(\mathbf{A_{11}}_{\text{ex}} + \mathbf{u_M^1} \mathbf{v_M^{1}}^T)$. Simplifying the result as far as possible, we finally arrive at

$$\frac{\det \mathbf{M_2}}{\det \mathbf{A}} = (\alpha_{11} - b_{11})(\alpha_{22} - b_{22}) - (\alpha_{12} - b_{12})(\alpha_{21} - b_{21}).$$

$$(\text{A11})$$

If we compare Eqs. (A9), it is clear that Eq. (A3) holds.

We now assume that for a certain value $n \in \mathbb{N}$ Eq. (A2) holds. For $n+1$, we can cast the matrix $\mathbf{M_{n+1}}$ in a form, where we can make use of Eq. (A2) holding for n,

$$\mathbf{M_{n+1}} = \begin{pmatrix} \widetilde{\mathbf{A}} & \widetilde{\mathbf{u}}_2 & \cdots & \widetilde{\mathbf{u}}_{n+1} \\ \widetilde{\mathbf{v}}_2^T & \alpha_{2,2} & \cdots & \alpha_{2,n+1} \\ \vdots & \vdots & \ddots & \vdots \\ \widetilde{\mathbf{v}}_n^T & \alpha_{n,2} & \cdots & \alpha_{n,n+1} \\ \widetilde{\mathbf{v}}_{n+1}^T & \alpha_{n+1,2} & \cdots & \alpha_{n+1,n+1} \end{pmatrix}, \quad (\text{A12})$$

where we have introduced the new matrix $\widetilde{\mathbf{A}}$ and the vectors $\widetilde{\mathbf{u}}_i$ and $\widetilde{\mathbf{u}}_j$ with

$$\widetilde{\mathbf{A}} = \begin{pmatrix} \mathbf{A} & \mathbf{u_1} \\ \mathbf{v_1}^T & \alpha_{11} \end{pmatrix}, \quad \widetilde{\mathbf{u}}_i = \begin{pmatrix} \mathbf{u_i} \\ \alpha_{1i} \end{pmatrix}, \quad \widetilde{\mathbf{v}}_i = \begin{pmatrix} \mathbf{v_i} \\ \alpha_{i1} \end{pmatrix}. \quad (\text{A13})$$

Further, we need the matrices $\widetilde{\mathbf{A}}_{ij}$ defined analogously to Eq. (A1),

$$\widetilde{\mathbf{A}}_{ij} = \begin{pmatrix} \widetilde{\mathbf{A}} & \widetilde{\mathbf{u}}_j \\ \widetilde{\mathbf{v}}_i^T & \alpha_{ij} \end{pmatrix} = \begin{pmatrix} \mathbf{A} & \mathbf{u_1} & \mathbf{u_j} \\ \mathbf{v_1}^T & \alpha_{11} & \alpha_{1j} \\ \mathbf{v_i}^T & \alpha_{i1} & \alpha_{ij} \end{pmatrix}. \quad (\text{A14})$$

With these definitions, and with the abbreviations $a_{ij} = \det \mathbf{A_{ij}}$ and $\widetilde{a}_{ij} = \det \widetilde{\mathbf{A}}_{ij}$, we are now able to apply Eq. (A2) holding for n,

$$\det \mathbf{M_{n+1}} (\det \widetilde{\mathbf{A}})^{(n-1)} = \det \begin{pmatrix} \widetilde{a}_{2,2} & \cdots & \widetilde{a}_{2,n+1} \\ \vdots & \ddots & \vdots \\ \widetilde{a}_{n+1,2} & \cdots & \widetilde{a}_{n+1,n+1} \end{pmatrix}.$$

$$(\text{A15})$$

For $\widetilde{a}_{ij}$, we make use of Eq. (A2) with $n=2$, which we have proved above

$$\widetilde{a}_{ij} = \frac{1}{\det \mathbf{A}} (a_{11} a_{ij} - a_{i1} a_{1j}). \quad (\text{A16})$$

Inserting this result in Eq. (A15) yields a determinant with entries of the form $a_{11} a_{ij} - a_{i1} a_{1j}$. We make use of the multilinearity of the determinant to decompose this expression and we obtain a sum of determinants with prefactors of the form a_{ij}. Eliminating zero contributions, the resulting expression corresponds precisely to the Laplace expansion of a larger determinant and we finally obtain

$$\det \mathbf{M_{n+1}} \det \mathbf{A}^n = \det \begin{pmatrix} a_{1,1} & a_{1,2} & \cdots & a_{1,n+1} \\ a_{2,1} & a_{2,2} & \cdots & a_{2,n+1} \\ \vdots & \vdots & \ddots & \vdots \\ a_{n+1,1} & a_{n+1,2} & \cdots & a_{n+1,n+1} \end{pmatrix}.$$

$$(\text{A17})$$

This is the identity [Eq. (A2)] for $n+1$. Hence we have derived the determinant identity for $n+1$ using only the identity for n and $n=2$. By induction, the identity [Eq. (A2)] therefore holds for every $n \in \mathbb{N}$, as it is trivial for $n=1$.

*dluitz@physik.uni-wuerzburg.de

[1] H. Shiba, Prog. Theor. Phys. **40**, 435 (1968).

[2] A. Sakurai, Prog. Theor. Phys. **44**, 1472 (1970).

[3] B. D. Josephson, Phys. Lett. **1**, 251 (1962).

[4] I. O. Kulik, Sov. Phys. JETP **22**, 841 (1966).

[5] L. I. Galzman and K. A. Matveev, JETP Lett. **49**, 659 (1989).

[6] B. I. Spivak and S. A. Kivelson, Phys. Rev. B **43**, 3740 (1991).

[7] A. Eichler, R. Deblock, M. Weiss, C. Karrasch, V. Meden, C. Schönenberger, and H. Bouchiat, Phys. Rev. B **79**, 161407 (2009).

[8] J.-P. Cleuziou, W. Wernsdorfer, V. Bouchiat, T. Ondarçuhu, and M. Monthioux, Nat. Nanotechnol. **1**, 53 (2006).

[9] H. I. Jørgensen, T. Novotný, K. Grove-Rasmussen, K. Flensberg, and P. E. Lindelof, Nano Lett. **7**, 2441 (2007).

[10] J. A. van Dam, Y. V. Nazarov, E. P. A. M. Bakkers, S. D. Franceschi, and L. P. Kouwenhoven, Nature (London) **442**, 667 (2006).

[11] K. Grove-Rasmussen, H. I. Jørgensen, and P. E. Lindelof, New J. Phys. **9**, 124 (2007).

[12] H. I. Jørgensen, K. Grove-Rasmussen, T. Novotný, K. Flensberg, and P. E. Lindelof, Phys. Rev. Lett. **96**, 207003 (2006).

[13] T. Sand-Jespersen, J. Paaske, B. M. Andersen, K. Grove-Rasmussen, H. I. Jørgensen, M. Aagesen, C. B. Sørensen, P. E. Lindelof, K. Flensberg, and J. Nygård, Phys. Rev. Lett. **99**, 126603 (2007).

[14] A. Eichler, M. Weiss, S. Oberholzer, C. Schönenberger, A. L. Yeyati, J. C. Cuevas, and A. Martín-Rodero, Phys. Rev. Lett. **99**, 126602 (2007).

[15] M. R. Buitelaar, T. Nussbaumer, and C. Schönenberger, Phys. Rev. Lett. **89**, 256801 (2002).

[16] M.-S. Choi, M. Lee, K. Kang, and W. Belzig, Phys. Rev. B **70**, 020502(R) (2004).

[17] A. Oguri, Y. Tanaka, and A. C. Hewson, J. Phys. Soc. Jpn. **73**, 2494 (2004).

[18] J. Bauer, A. Oguri, and A. C. Hewson, J. Phys.: Condens. Matter **19**, 486211 (2007).

[19] T. Hecht, A. Weichselbaum, J. von Delft, and R. Bulla, J. Phys.: Condens. Matter **20**, 275213 (2008).

[20] F. Siano and R. Egger, Phys. Rev. Lett. **93**, 047002 (2004).

[21] F. Siano and R. Egger, Phys. Rev. Lett. **94**, 039902(E) (2005).

[22] F. Siano and R. Egger, Phys. Rev. Lett. **94**, 229702 (2005).

[23] C. Karrasch, A. Oguri, and V. Meden, Phys. Rev. B **77**, 024517 (2008).

[24] A. N. Rubtsov, V. V. Savkin, and A. I. Lichtenstein, Phys. Rev. B **72**, 035122 (2005).

[25] A. A. Clerk and V. Ambegaokar, Phys. Rev. B **61**, 9109 (2000).

[26] A. V. Rozhkov and D. P. Arovas, Phys. Rev. B **62**, 6687 (2000).

[27] E. Vecino, A. Martín-Rodero, and A. Levy Yeyati, Phys. Rev. B **68**, 035105 (2003).

[28] T. Meng, S. Florens, and P. Simon, Phys. Rev. B **79**, 224521 (2009).

[29] A. Georges, G. Kotliar, W. Krauth, and M. J. Rozenberg, Rev. Mod. Phys. **68**, 13 (1996).

[30] M. I. Salkola, A. V. Balatsky, and J. R. Schrieffer, Phys. Rev. B **55**, 12648 (1997).

[31] A. V. Balatsky, I. Vekhter, and J.-X. Zhu, Rev. Mod. Phys. **78**, 373 (2006).

[32] A. C. Hewson and D. Edwards, *The Kondo Problem to Heavy Fermions*, Cambridge Studies in Magnetism (Cambridge University Press, Cambridge, London, 2003).

[33] F. F. Assaad and T. C. Lang, Phys. Rev. B **76**, 035116 (2007).

[34] A. V. Rozhkov and D. P. Arovas, Phys. Rev. Lett. **82**, 2788 (1999).

[35] C. Benjamin, T. Jonckheere, A. Zazunov, and T. Martin, Eur. Phys. J. B **57**, 279 (2007).

[36] A. W. Sandvik, Phys. Rev. B **57**, 10287 (1998).

[37] K. S. D. Beach, arXiv:cond-mat/0403055 (unpublished).

[38] The dynamical charge structure factor itself can, in principle, be calculated from the CTQMC result for the charge correlation function $C_c(\tau) = \langle \tilde{n}(\tau)\tilde{n} \rangle - \langle \tilde{n} \rangle \langle \tilde{n} \rangle$ using stochastic analytic continuation. This, however, is numerically demanding and requires a very high quality of data. In the present case, we were unable to extract more than the lowest lying excitation of the dynamical charge structure factor, which is directly connected to the charge gap. The higher energy spectrum showed an extremely complex structure which is difficult to capture with stochastic analytic continuation.

[39] Strictly speaking, the reference model in the DMFT only has one superconducting bath while we introduced a left bath and a right bath in Hamiltonian (1). However, in the CTQMC, the reference model is entirely encoded in the bare Green's function, which can be understood as an action representation in the path-integral formalism. The explicit number of the superconducting baths is therefore unimportant.

[40] J. Bauer and A. C. Hewson, EPL **85**, 27001 (2009).

[41] J. Bauer, A. C. Hewson, and N. Dupuis, Phys. Rev. B **79**, 214518 (2009).

[42] G. Kotliar and A. E. Ruckenstein, Phys. Rev. Lett. **57**, 1362 (1986).